

UNIVERSITÀ DEGLI STUDI DI MILANO



Facoltà di Scienze MM.FF.NN.

Dipartimento di Chimica Fisica ed Electrochimica

Corso di Dottorato di Ricerca in SCIENZE CHIMICHE - CHIM/02

**CHALLENGING QUESTIONS IN CHEMISTRY:  
THE SYNERGIC ROLE OF *AB-INITIO* CALCULATIONS,  
X-RAY DERIVED CHARGE DENSITIES AND MODERN  
TOPOLOGICAL APPROACHES TO BONDING**

Relatore: Dr. Leonardo Lo Presti

Correlatore: Dr. Carlo Gatti

Coordinatore del Corso di Dottorato: Prof. Silvia Ardizzone

Tesi di Dottorato di Ricerca di:  
Simone Cenedese  
Matr. R08325

Anno Accademico 2010-2011

# Index

<b>Chapter 1: Introduction</b>	pag. 1
<b>Chapter 2: FeX<sub>2</sub> (X = S, P, As, Sb) marcasitic compounds</b>	pag. 3
1. Introduction	pag. 3
2. Marcasites crystallographic structure	pag. 3
2.1. Local geometric structure, <i>d</i> -orbital splitting and formal charge of iron	pag. 6
3. Computational details	pag. 9
4. Results	pag. 11
4.1. Electronic structure: dependency from the level of theory	pag. 11
4.2. Electronic structure: orbital-based analysis	pag. 18
4.3. Electronic structure: observable-based analysis	pag. 22
5. Conclusions	pag. 35
<b>Chapter 3: Hypervalency in K<sub>2</sub>SO<sub>4</sub></b>	pag. 38
1. Introduction	pag. 38
2. Computational details	pag. 41
3. Results and Discussion	pag. 41
4. Conclusions	pag. 54
<b>Chapter 4: Coordination Polymers: the case of [Zn(HCOO)<sub>2</sub>(H<sub>2</sub>O)<sub>2</sub>]<sub>∞</sub></b>	pag. 56
1. Introduction	pag. 56
2. Crystallographic structure	pag. 57
3. Computational details	pag. 58
4. Results and Discussion	pag. 59
5. Conclusions	pag. 65
<b>Chapter 5: Conclusions and Future Work</b>	pag. 67
<b>References</b>	pag. 69

## Chapter 1

### Introduction

During the last 20 years the analysis of the charge density has grown from a small area of research reserved for scientists almost exclusively devoted to this field to quite a routine technique. Many books have been devoted to this field and it is common nowadays working with instruments and program packages designed for collect, refine and model the electron density almost without the help of an external user. In some cases, the same can be said also when thinking at the charge density derived from *ab-initio* calculations.

Nonetheless, many issues still exist that makes this analysis less of a routine a more real scientific work. Thinking at the problems one can encounter when performing XRD measurements and refining diffraction data, it is possible to cite the presence of heavy elements in the structure, high symmetry, extinction effects, static and dynamic disorder. There are cases in which these problems can be overcome or, at least, minimized, but still there's a huge number of chemical systems for which ambiguities and (sometimes) contradictory outcomes result from the experimental analysis alone (especially for what concerns bonding and not just structure).

This work deals with the role *ab-initio* calculations have in supporting and, when needed, helping to clarify the meaning of experimental findings. Furthermore, the extra information one gets from the wavefunction, that is the knowledge of the density matrix and of the pair density, both customarily unavailable from experiment, has revealed of uttermost importance in the study of the challenging chemical bond features investigated in this thesis.

This work is the result of a strong and still ongoing collaboration with the "Charge Density" group at the University of Århus (Denmark), whose members were responsible of the collection, reduction, and analysis of the experimental data. In particular, PhD student Mette S. Schmøkel

followed the work on  $K_2SO_4$  and is currently working on  $FeX_2$  marcasitic systems, and PhD student Mads R. V. Jørgensen the work on transition metal formates.

## Chapter 2

# FeX<sub>2</sub> (X = S, P, As, Sb) marcasitic compounds

### 1. Introduction

Marcasite type structures have recently received huge interest since it was discovered that FeSb<sub>2</sub> exhibits a colossal thermoelectric power factor at low temperature,<sup>1,2</sup> and if the thermal conductivity can be lowered the material holds the potential for providing an efficient cooling technology e.g. for superconducting transmission cables. The extraordinary physical properties are still not well understood<sup>3</sup> and clearly it is of fundamental interest to examine in depth the crystal structure, electronic structure and chemical bonding.

In the next paragraphs, the electronic structure for marcasites (*M*) and löllingites (*L*) is revised and it will be shown how geometry, electronic structure and bonding interactions are intriguingly interplayed in such compounds. The predictions of ligand field theory (LFT) are compared with the *ab-initio* orbital-based view of both the anisotropy of the iron *d*-electrons distribution and the composition of bonding and antibonding states close to the Fermi level. The orbital-based picture is tested against the study of the charge transfer, the nature of the bonding interactions and the valence anisotropy of the iron atom using the topology of two observables, the electron density,  $\rho$  and its Laplacian,  $\nabla^2 \rho$  within the Quantum Theory of Atoms In Molecules (QTAIM).

### 2. Marcasites crystallographic structure

The crystallographic structures of marcasite type compounds were extensively scrutinized in a series of studies around 1970.<sup>4,5,6,7,8</sup> The binary compounds TX<sub>2</sub> (T = transition metal, X group XV or XVI element) that belong to the marcasite type structure crystallize in the *Pnmm* space group (#58) and have two formula units in the unit cell (Figure 2.1). Within this crystal structure,

however, two distinct groups of compounds, sharing the same space group, but distinguished according to the ratios  $c/a$  and  $c/b$  of the cell parameters, can be identified. *Marcasites* (*M*), for which the reference compound is  $\text{FeS}_2$ , exhibit  $c/a$  and  $c/b$  values close to 0.74 and 0.62, respectively. On the other hand, significantly lower ratios, typically 0.55 ( $c/a$ ) and 0.48 ( $c/b$ ), are found in *löllingites* (*L*), whose standard reference compound is  $\text{FeAs}_2$ . Other definitions, reported in Table 2.1, appeared in literature from time to time. The terms marcasite and löllingite refer to the mineralogical definition and will be adopted in the following.

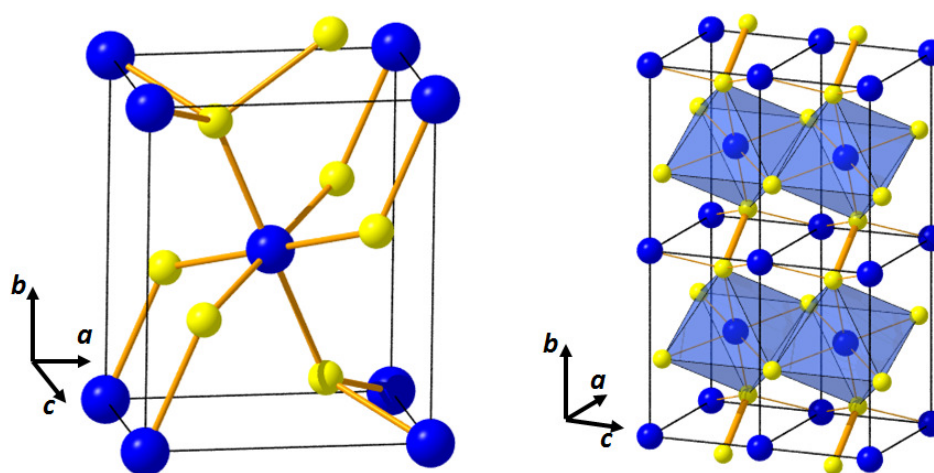


**Figure 2.1**  $\text{TX}_2$  marcasite type crystal structure. Left: each T atom (blue) is coordinated with six X atoms (yellow) in an octahedral environment; each X atom is surrounded by three T and one X atoms placed at the corners of a tetrahedron (shown only for the X atom in the top-left part of the cell, for the sake of clarity). Right:  $\text{TX}_6$  octahedra are connected along  $a$  and  $b$  axes through  $\text{X}_2$  dumbbells (only those along  $b$  are shown in the figure), while along  $c$  they are edge-sharing.

**Table 2.1** Proposed nomenclature, based on the basis of the cell parameters ( $c/a$  and  $c/b$ ) ratio, for the two different groups of compounds belonging to the marcasite type structure.

$c/a$	$c/b$	Definitions
0.74	0.62	marcasites
		anomalous marcasites
		normal marcasites
0.55	0.48	löllingites
		Jahn-Teller marcasites
		compressed marcasites
		regular marcasites

Two main differences can thus be highlighted between *L* and *M* types of compounds: a geometric one, due to the notable compression along the *c* axis in the former, and an electronic one, given by the two less valence electrons per formula unit characterizing *L* rather than *M* type structure.

Iron disulphide is the leading term of marcasites and the *M* structure is retained also when sulphur is replaced with other group VI elements like Se and Te. When substituting chalcogen atoms with group V ones, i.e. removing 2 e<sup>-</sup>/formula unit, the löllingite structure comes into being (Table 2.2).

**Table 2.2** TX<sub>2</sub> (T = Fe, Ni ; X = P, As, Sb, S, Se, Te) marcasite- and löllingite-type compounds. Cell parameters *a*, *b* and *c* are given in Ångstrom, while the Fe-X-Fe angle along the *c* axis ( $\delta$ , see also Figure 2.3) is given in degrees. The cell parameters (*c/a* and *c/b*) ratios are also shown for each compound in the table.

	Marcasite-type			Löllingite-type	
FeS <sub>2</sub> <sup>6,8</sup>	<i>a</i> = 4.4431 Å	<i>c/a</i> = 0.76	FeP <sub>2</sub> <sup>5</sup>	<i>a</i> = 4.9729 Å	<i>c/a</i> = 0.55
	<i>b</i> = 5.4245 Å	<i>c/b</i> = 0.62		<i>b</i> = 5.6568 Å	<i>c/b</i> = 0.48
	<i>c</i> = 3.3871 Å	$\delta$ = 97.4°		<i>c</i> = 2.7230 Å	$\delta$ = 73.9°
FeSe <sub>2</sub> <sup>9</sup>	<i>a</i> = 4.8002 Å	<i>c/a</i> = 0.75	FeAs <sub>2</sub> <sup>9</sup>	<i>a</i> = 5.3012 Å	<i>c/a</i> = 0.54
	<i>b</i> = 5.7823 Å	<i>c/b</i> = 0.62		<i>b</i> = 5.9858 Å	<i>c/b</i> = 0.48
	<i>c</i> = 3.5834 Å	$\delta$ = 97.5°		<i>c</i> = 2.8822 Å	$\delta$ = 74.3°
FeTe <sub>2</sub> <sup>10,6</sup>	<i>a</i> = 5.2655 Å	<i>c/a</i> = 0.74	FeSb <sub>2</sub> <sup>10,11</sup>	<i>a</i> = 5.8328 Å	<i>c/a</i> = 0.55
	<i>b</i> = 6.2679 Å	<i>c/b</i> = 0.62		<i>b</i> = 6.5376 Å	<i>c/b</i> = 0.49
	<i>c</i> = 3.8738 Å	$\delta$ = 97.8°		<i>c</i> = 3.1973 Å	$\delta$ = 76.0°
NiAs <sub>2</sub> <sup>9</sup>	<i>a</i> = 4.7582 Å	<i>c/a</i> = 0.74	FeAs <sub>2</sub> <sup>9</sup>	<i>a</i> = 5.3012 Å	<i>c/a</i> = 0.54
	<i>b</i> = 5.7949 Å	<i>c/b</i> = 0.61		<i>b</i> = 5.9858 Å	<i>c/b</i> = 0.48
	<i>c</i> = 3.5440 Å	$\delta$ = 95.5°		<i>c</i> = 2.8822 Å	$\delta$ = 74.3°
NiSb <sub>2</sub> <sup>9</sup>	<i>a</i> = 5.1823 Å	<i>c/a</i> = 0.74	FeSb <sub>2</sub> <sup>10,11</sup>	<i>a</i> = 5.8328 Å	<i>c/a</i> = 0.55
	<i>b</i> = 6.3168 Å	<i>c/b</i> = 0.61		<i>b</i> = 6.5376 Å	<i>c/b</i> = 0.49
	<i>c</i> = 3.8403 Å	$\delta$ = 96.7°		<i>c</i> = 3.1973 Å	$\delta$ = 76.0°

This consideration holds also upon substitution of the cation. When Fe is replaced by Ni in FeAs<sub>2</sub> and FeSb<sub>2</sub> the corresponding marcasites are obtained (Table 2.2). NiP<sub>2</sub>, on the contrary, crystallize in the *Pa*3 space group, retaining the NiS<sub>2</sub> pyrite crystal structure. It must be noted however that pyrite is also the most stable polymorph of FeS<sub>2</sub>. The removal of just 1 e<sup>-</sup>/formula unit from the marcasite structure involves major structural modifications leading to the monoclinic arsenopyrite structure, space group *P*2<sub>1</sub>/*c* (#14). The leading term is the ternary compound FeAsS, clearly

highlighting the intermediate composition between FeS<sub>2</sub> and FeAs<sub>2</sub>. However, also the binary ones exist, having CoSb<sub>2</sub> as leading term.

The present study focuses on examining some of the representatives of the marcasites and löllingites families: FeS<sub>2</sub>, FeP<sub>2</sub>, FeAs<sub>2</sub> and FeSb<sub>2</sub>.

## 2.1. Local geometric structure, *d*-orbital splitting and formal charge of iron

According to Goodenough,<sup>12</sup> who critically reviewed the conjecture proposed by Hullinger & Mooser<sup>13</sup> and the expansion model proposed by Brostigen & Kjekshus,<sup>6</sup> the the electronic structure of these compounds can be rationalized considering the distorted octahedral environment of the transition metal. The analysis has been conducted considering mainly FeS<sub>2</sub>, FeAsS and FeAs<sub>2</sub>, and subsequently generalized to TX<sub>2</sub> marcasites. It requires a proper choice of the reference system: of the six Fe-X interatomic distances, two are shorter than the other four: the *z* axis is aligned along the short Fe-X interactions (*axial*) while the *x* and *y* axes, which point approximately along the longest bonds (*equatorial*), are rotated so as to be equidistant from the internuclear axes of such bonds. Also in the following, when Mulliken charges and orbital-projected DOS referring to specific orbitals (like *d<sub>xy</sub>* or *p<sub>z</sub>*, for example) will be discussed, they were all obtained using the aforementioned “chemical reference system” for the various compounds.

According to the ligand field theory (LFT), in a perfect octahedral environment the five 3*d* orbital of the metal atom are split into the three *t<sub>2g</sub>* orbitals (*d<sub>xy</sub>*, *d<sub>yz</sub>*, *d<sub>xz</sub>*) of lower energy and two *e<sub>g</sub>* orbitals (*d<sub>x<sup>2</sup>-y<sup>2</sup></sub>*, *d<sub>z<sup>2</sup></sub>*) of higher energy. This splitting stems from the fact that the latter orbitals point directly towards the negatively charged ligands whereas the former are directed in between them. In our case, a further increase in the energy of the *d<sub>z<sup>2</sup></sub>* orbital is expected since the axial interactions are shorter than the equatorial ones. Furthermore, in the equatorial plane, the X ligands approach the Fe atom with angles different from 90°, so that a lowering of *d<sub>x<sup>2</sup>-y<sup>2</sup></sub>* and a rising of *d<sub>xy</sub>*, with respect to

the LFT ideal octahedral splitting is expected. These considerations lead to the scheme depicted in Figure 2.2 for Fe *d*-orbitals splitting.

As previously mentioned, geometrical distortions lead to *x* and *y* axes that are not perfectly aligned with the Fe-X equatorial interactions (Figure 2.3 and Table 2.3).

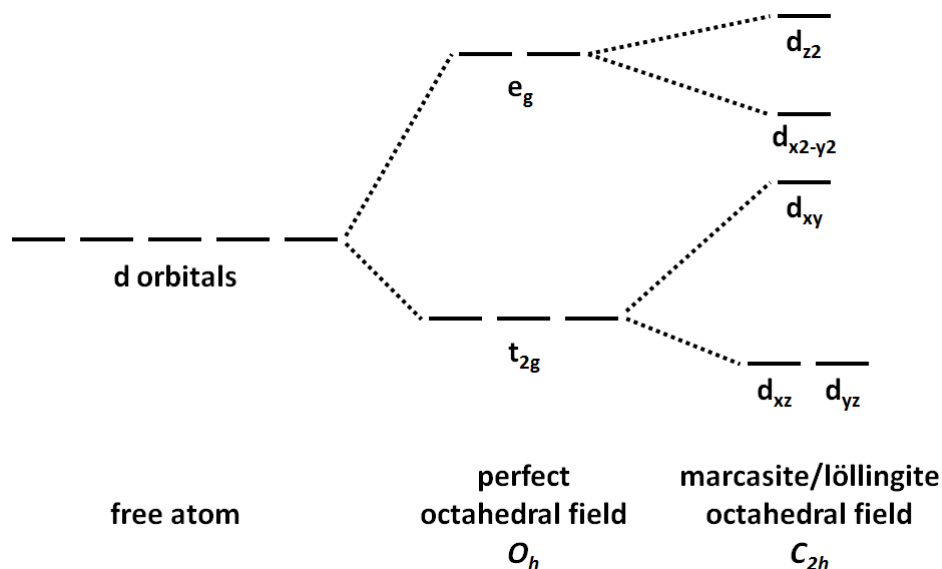


**Figure 2.2** Splitting scheme for iron *d*-orbitals in the case of the free atom (left), for a perfect octahedral environment (middle) and in the case of the distorted octahedral field in marcasite and löllingite type of structure (right). The separation between the orbitals is purely qualitative and doesn't rely on energy calculations.

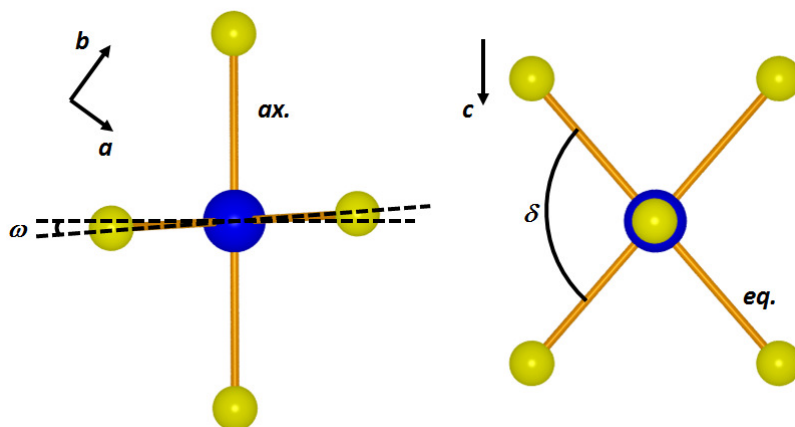


**Figure 2.3** TX<sub>6</sub> octahedra structure: left) seen along the *c* axis: the two axial (ax.) T-X interactions and the tilting (angle  $\omega$ ) of the equatorial plane with respect to them. right) down the *c* axis: the four equatorial (eq.) T-X interactions and the angle  $\delta$ , which is related to the compression of the *c* axis on passing from *M* to *L*. See Table 2.3 for numerical values.

**Table 2.3** FeX<sub>2</sub> (X=S,P) lattice and geometrical parameters for the experimental (exp) and optimized (opt) structures valuated with the PBE and B3PW functionals. The values in parentheses (for PBE) refer to the most contracted basis set, optimized for B3PW.

		FeS <sub>2</sub>	FeP <sub>2</sub>	FeAs <sub>2</sub>	FeSb <sub>2</sub>	
exp	a (Å)	4.4431	4.9729	5.3012	5.8328	
	b (Å)	5.4245	5.6568	5.9858	6.5376	
	c (Å)	3.3871	2.7230	2.8822	3.1973	
	Fe-X ax. (Å)	2.2359	2.2484	2.3620	2.5746	
	Fe-X eq. (Å)	2.2539	2.2637	2.3874	2.5965	
	X-X (Å)	2.2154	2.2365	2.4915	2.8941	
	δ (degrees)	97.4	73.9	74.3	76.0	
	ω (degrees)	1.9	1.9	1.9	1.7	
opt (PBE)	a (Å)	4.4426 (4.4759)	4.9758 (4.9988)	5.3122 (5.2992)	5.9236 (5.7997)	
	b (Å)	5.4114 (5.3939)	5.6529 (5.6571)	5.9772 (5.9872)	6.6050 (6.4877)	
	c (Å)	3.3956 (3.3813)	2.7233 (2.7087)	2.8802 (2.8826)	3.1156 (3.2398)	
	Fe-X ax. (Å)	2.2311 (2.2240)	2.2444 (2.2460)	2.3625 (2.3584)	2.6216 (2.5654)	
	Fe-X eq. (Å)	2.2464 (2.2414)	2.2594 (2.2616)	2.3813 (2.3837)	2.5915 (2.5852)	
	X-X (Å)	2.2613 (2.3036)	2.2610 (2.2681)	2.5135 (2.5148)	2.8930 (2.9065)	
	δ (degrees)	98.2 (97.9)	74.1 (73.6)	74.4 (74.4)	73.9 (77.6)	
	ω (degrees)	1.9 (1.7)	1.9 (1.8)	1.7 (1.9)	1.2 (1.4)	
	opt (B3PW)	a (Å)	4.4392	4.9590	5.2506	5.7538
		b (Å)	5.4081	5.6961	6.0333	6.5447
c (Å)		3.4003	2.7117	2.8870	3.2374	
Fe-X ax. (Å)		2.2419	2.2747	2.3924	2.6009	
Fe-X eq. (Å)		2.2645	2.2461	2.3673	2.5696	
X-X (Å)		2.1484	2.2463	2.4801	2.8723	
δ (degrees)		97.3	74.3	75.1	78.1	
ω (degrees)	1.6	1.9	2.2	1.7		

Central to almost any assumption on the electronic structure of these compounds, is that both *M* and *L* structures are characterized by noninteracting diatomic anions (X<sub>2</sub>)<sup>n-</sup>. Assuming the presence of one X-X bond per formula unit, the formal charges of the anion are n = 2 or 4 for chalcogen and pnictogen ligand, respectively. For iron compounds, this would result in a formal charge of +2 and

+4, respectively, for Fe in a fully ionic description. However, this picture is hardly supported by the known similarity of Pauling electronegativity values (Table 2.4) nor is by the observation that chalcogen atoms have an higher electronegativity value than pnictogen ones, which makes the predicted trend of formal charges of iron by the fully ionic description even more unrealistic.

**Table 2.4** Pauling electronegativities ( $\chi$ ) and electronegativity differences for Fe, pnictogen ( $X_{\text{pnict.}}$  = P, As, Sb) and chalcogen ( $X_{\text{chalc.}}$  = S, Se, Te) elements.

$\chi(\text{Fe})$		$\chi(X_{\text{pnict.}})$		$\chi(\text{Fe}) - \chi(X_{\text{pnict.}})$		$\chi(X_{\text{chalc.}})$		$\chi(\text{Fe}) - \chi(X_{\text{chalc.}})$	
<i>Fe</i>	1.83	<i>P</i>	2.19	0.36	<i>S</i>	2.58	0.75		
		<i>As</i>	2.18	0.35	<i>Se</i>	2.55	0.72		
		<i>Sb</i>	2.05	0.22	<i>Te</i>	2.10	0.27		

In a recent paper<sup>14</sup> a different view was suggested for FeSb<sub>2</sub>. Instead of considering the Sb<sub>2</sub> pairs as noninteracting units, they could be considered as the rungs of an infinite ladder running trough *c* axis in the crystal, the ladder being the result of the coupling of two infinite linear Sb chains due to Peierls distortion. Doing so results in Sb holding a -1 formal charge and, as a consequence, a more conventional +2 state for iron, consistent with the 18 electrons rule. The same approach has been recently adopted for the analysis of MN<sub>2</sub> (M = Ir, Os, Rh) transition metal nitrides.<sup>15</sup> However, the authors themselves acknowledge that this analysis cannot be generalized and used to explain the formal oxidation states of the other compounds. For NiSb<sub>2</sub>, for example, taking into account Peierls distortion results again in a +2 formal charge for the metal but then Sb<sub>2</sub> pairs would be characterized by a Sb-Sb double bond. The presence of such a bond, on the other side, in the case of isolated Sb<sub>2</sub> pairs would lead to an unusual +4 oxidation state for Ni.

### 3. Computational details

The results reported here have been obtained via periodic ab-initio Density Functional Theory (DFT) calculations employing the CRYSTAL06 code.<sup>16</sup> Mainly all electron def2-TZVP basis sets

<sup>17,18</sup> have been used.<sup>a</sup> For FeSb<sub>2</sub> a description based on small-core (16 and 23 electrons explicitly described for Fe and Sb respectively) pseudo-potentials has also been considered.<sup>19</sup> Due to the diffuseness of the outer functions of such basis sets, it was not possible to use the original basis set formulation in the CRYSTAL code. In general, the most diffuse functions were cut while the Gaussian exponents of the remaining valence functions on iron were recalculated according to the empirical “1/3” rule [ref. 16, Chapter 7]. Finally, the valence functions have been optimized in the crystal [ref. 16, Chapter 7] for the various basis sets and the considered DFT functionals, PBE and B3PW.<sup>20,21</sup> This resulted in more contracted basis set to be used with the B3PW functional.

As recommended for heavy atoms,<sup>16</sup> extra-large grids (keyword XLGRID in the CRYSTAL code) were used for the numerical evaluation of the exchange-correlation potential and energy. They consist of atom-centered contributions with 75 radial points, covering a range of 4.0 ionic radii, and 974 angular points. Wavefunctions, density of states (DOS) and all the other one-electronic properties obtained from the wavefunction were obtained using a shrinking factor of 12 for reciprocal space sampling according to the Pack-Monkhorst method, and of 24 for defining the Gilat net, used in the interpolation of the density matrix and the evaluation of the Fermi energy. This results in a total of 343 and 2197 sampling points in the Pack-Monkhorst and in the Gilat nets, respectively. Truncation thresholds were set to  $10^{-9}$ ,  $10^{-9}$ ,  $10^{-9}$ ,  $10^{-9}$  and  $10^{-18}$  a.u. (hartree) for the Coulomb and exchange series and to  $10^{-7}$  a.u. for the Self Consistent Field (SCF) convergence (total energy and eigenvalues).

Both the experimental and optimized geometries were considered for each investigated structure. A full optimization of cell parameters and atomic coordinates was performed within the *Pnmm* space group while freezing the cell volume at the experimental values (Table 2.1).

---

<sup>a</sup> It should be noted that Sb def2-TZVP basis set is not an “all-electron” since it relies on a pseudo-potential. For this reason an older TZVP formulation has been considered for Sb basis set.

## 4. Results

The DOS displayed in Figure 2.4 shows that, as expected, the region near the Fermi Level (FL) is dominated by the interactions between Fe and X, with the contribution from the metal atom being larger than that from the X atoms for both compounds below the FL. Above, but close to the FL, the DOS of the conduction bands show an almost similar trend for löllingites, whereas comparable contributions from Fe and S are found for FeS<sub>2</sub>. DOS projected on the atomic orbital subsets of Fe and X (Figure 2.5) reveal that the Fe-X interaction is essentially due to Fe *d* and X *p* states for both FeS<sub>2</sub> and FeP<sub>2</sub>, with the weight of X *p* states around the FL being smaller for valence than conduction bands in the former and the opposite being true in the latter compound.

### 4.1. Electronic structure: dependency from the level of theory

All the studied FeX<sub>2</sub> compounds are reported to be small gap diamagnetic conductors. Considering the estimated band gap values (Table 2.5), when the PBE functional is employed a good agreement with the reported experimental value (0.37eV) is found for FeP<sub>2</sub>.<sup>22</sup> To our knowledge, no experimental data are available for FeS<sub>2</sub>,<sup>23</sup> yet our computed value favorably compares with the previous ab-initio estimate (0.91 eV).<sup>23</sup> For FeAs<sub>2</sub> a band gap of 0.20eV is generally reported,<sup>24</sup> while for FeSb<sub>2</sub> values ranging from 0.3eV to 0.1eV can be found<sup>25, 26, 27</sup>, the situation being further complicated by the presence of smaller indirect gaps, causing a non-zero DOS at the Fermi level.<sup>28</sup> This could also be the case, as can be seen from the Density of States (DOS) in Figure 2.4 and, more clearly, from the bandwidth in Figure 2.6.

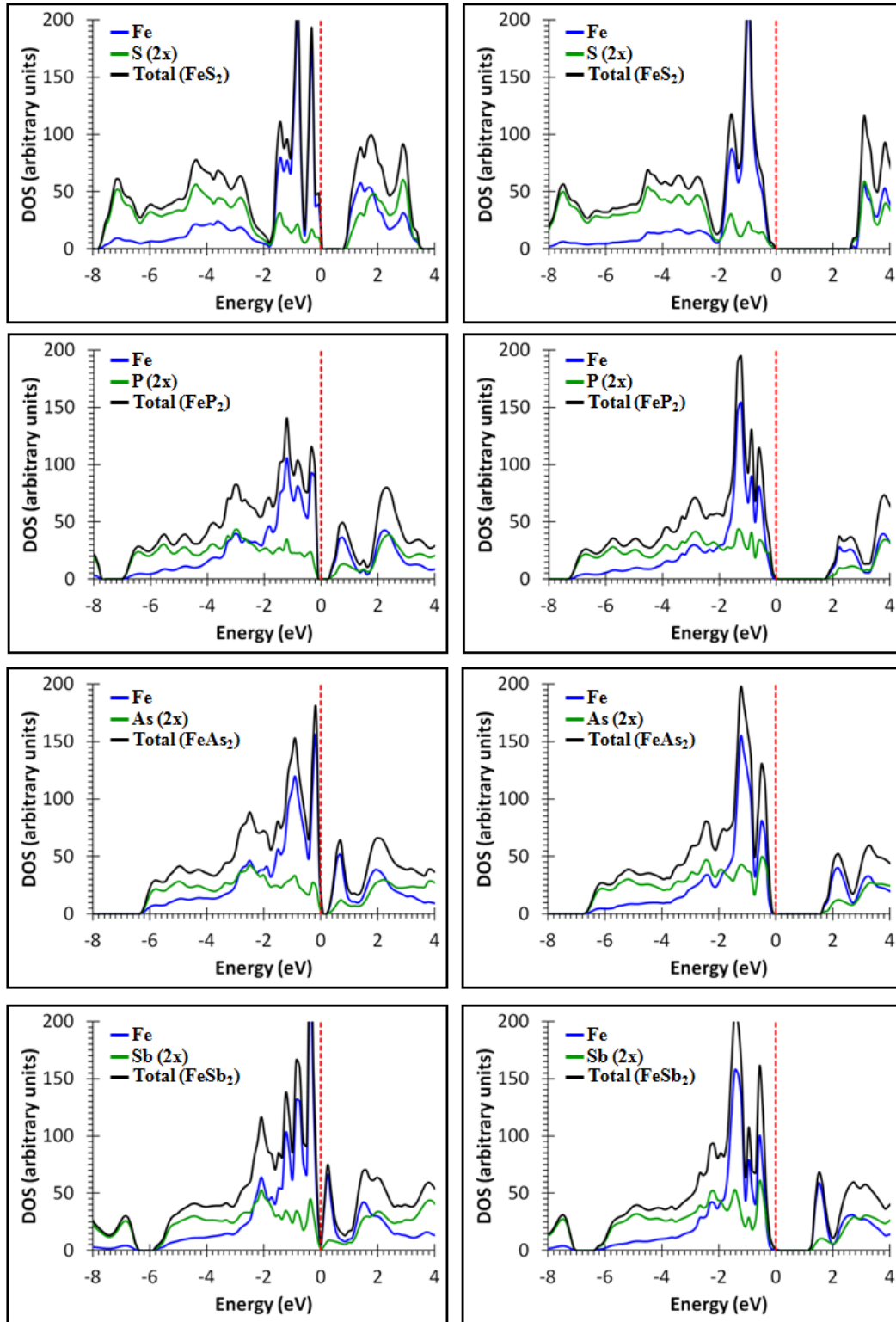


**Figure 2.4** Density Of States (DOS) for the  $\text{FeX}_2$  ( $X = \text{S}, \text{P}, \text{As}, \text{Sb}$ ) structures at the experimental geometry evaluated with the PBE (left) and B3PW (right) functionals. For each structure, the total and the atom-projected DOS (pDOS) are shown in the top panels. The Fermi Level is indicated by the dashed vertical red line in all plots.

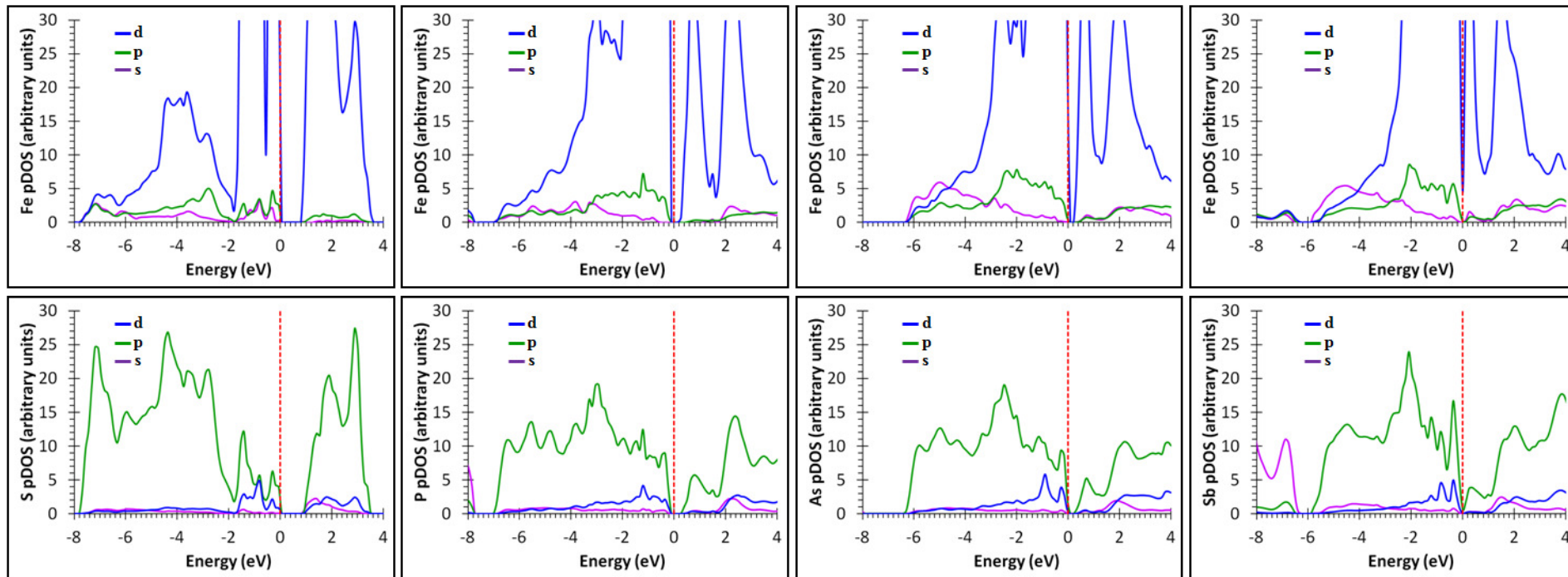


**Figure 2.5** Projected Density Of States (pDOS) for the  $\text{FeX}_2$  ( $X = \text{S}, \text{P}, \text{As}, \text{Sb}$ ; from left to right) structures at the experimental geometry evaluated with the PBE functional. For each structure, the top and bottom panels display the DOS projected on the atomic orbital subsets for Fe and X respectively.

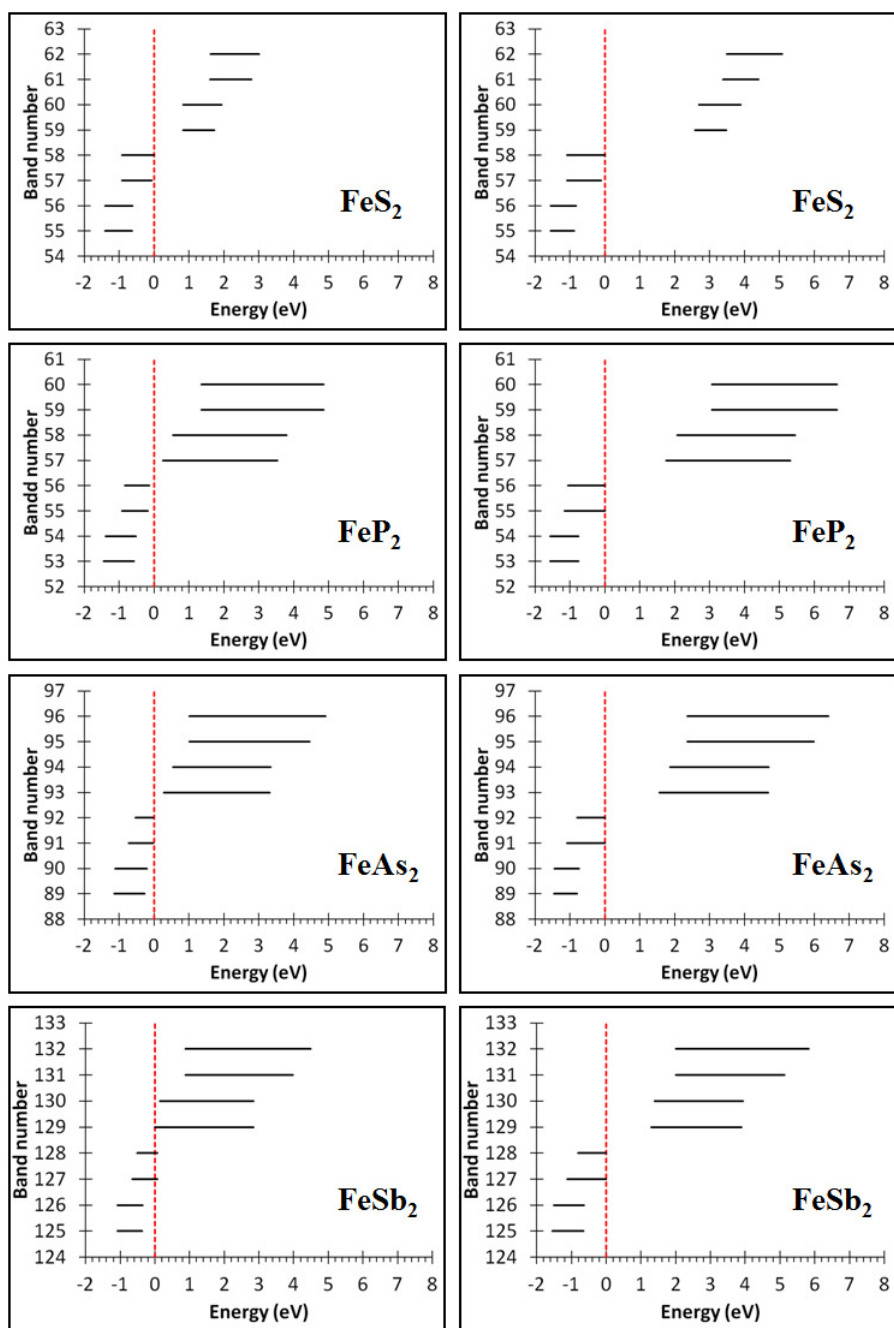


**Figure 2.6** Bandwidth for the  $\text{FeX}_2$  ( $X = \text{S}, \text{P}, \text{As}, \text{Sb}$ ) structures at the experimental geometry evaluated with the PBE (left) and B3PW (right) functionals.

**Table 2.5** Band gap values, reported in eV, evaluated for the experimental (exp) and optimized (opt) structures. The two values reported for the PBE basis set refer to the adoption of the two TZ basis sets considered with this functional: the PBE-optimized one (first line, roman) and the B3PW-optimized one (second line, italics)

	FeS <sub>2</sub>		FeP <sub>2</sub>		FeAs <sub>2</sub>		FeSb <sub>2</sub>	
	exp	Opt	exp	opt	exp	opt	exp	opt
PBE	0.83	0.87	0.39	0.41	0.30	0.28	-0.07	-0.07
	<i>0.83</i>	<i>0.83</i>	<i>0.42</i>	<i>0.42</i>	<i>0.29</i>	<i>0.29</i>	<i>-0.02</i>	<i>-0.09</i>
B3PW	2.58	2.82	1.75	1.77	1.57	1.55	1.30	1.22

On the other side, when considering the B3PW functional, all the compounds are described as insulating systems albeit at the price of a too wide separation between valence and conduction bands. This difference could be related to the different level of theory adopted for the calculation, and in particular to:

- a) the different diffuseness of the atomic basis set employed with PBE and B3PW.
- b) the inclusion of exchange energy in the formulation of the functional, since it is completely neglected in PBE while included as 20% of the exact HF estimate in B3PW.
- c) the inadequacy of an “all-electron” description when heavy atoms are considered, since relativistic corrections are customarily included only in pseudo-potential approaches

The issue related to point a) could be of concern for all the considered compounds. Considering the optimized structures (Table 2.3) it can be seen how PBE is almost always superior to B3PW in reproducing the lattice parameters and bond distances for the various compounds. The most contracted basis set, along with the PBE functional, is the best choice when dealing with the most diffuse atoms, As and Sb. For FeSb<sub>2</sub> in particular, this is the only case where, after the optimization procedure, the Fe-Sb axial bond is shorter than the equatorial one, as found experimentally.

Despite the aforementioned geometrical differences, negligible changes have been found for the band gap values (Table 2.5) as well as for the DOS pictures (not shown).

The percentage of Hartree-Fock exact exchange,  $\%HF_{ex}$ , added to the functional is instead found to have a much greater impact on the separation between valence and conduction band. The impact of this quantity on the electronic structure of a given compound is not surprising. It is not uncommon to screen different  $\%HF_{ex}$  values, in conjunction with a given DFT functional, in order to obtain the best description of a given property of a compound.  $FeSb_2$  (experimental geometry) has been here considered as the reference for this kind of analysis. Indeed an increase of the  $\%HF_{ex}$  included in the functional is found to enhance the separation between occupied and empty states (Figure 2.7 and Figure 2.8). In particular, lowering the  $\%HF_{ex}$  to 5% in B3PW, while raising it to the same amount in PBE, results in band gaps of 0.22eV and 0.14eV respectively, in good agreement with the experimental findings.

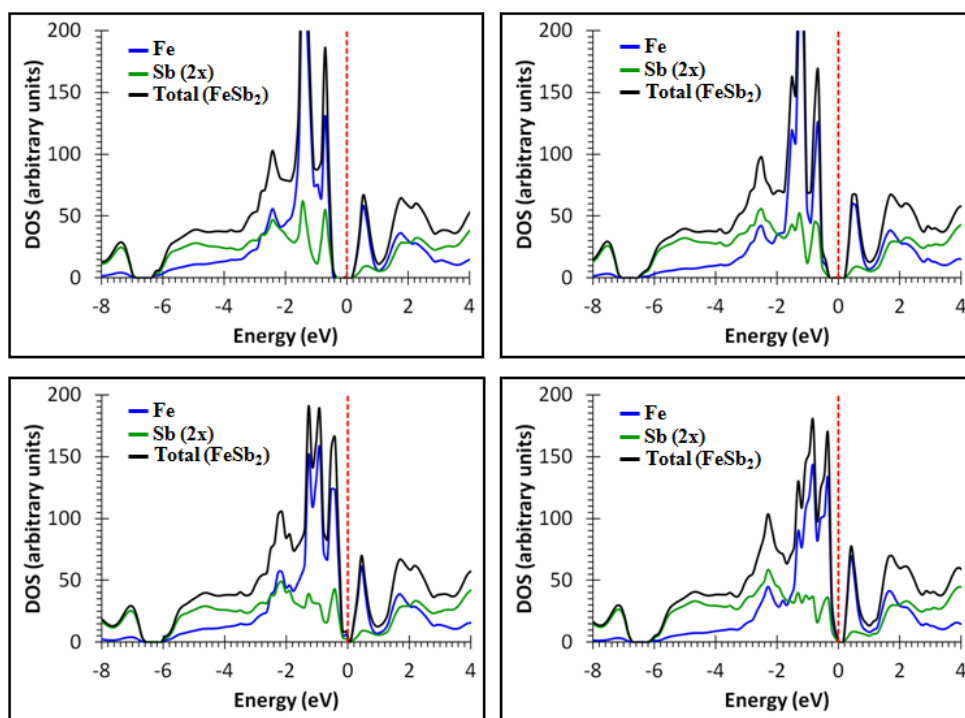


**Figure 2.7** Density Of States (DOS) for  $FeSb_2$  at the experimental geometry evaluated with the PBE (left) and B3PW (right) functionals (TZ basis set) and considering different amount of  $\%HF_{ex}$  (Top: 10%; Bottom: 5%). For each structure, the total and the atom-projected DOS (pDOS) are shown.

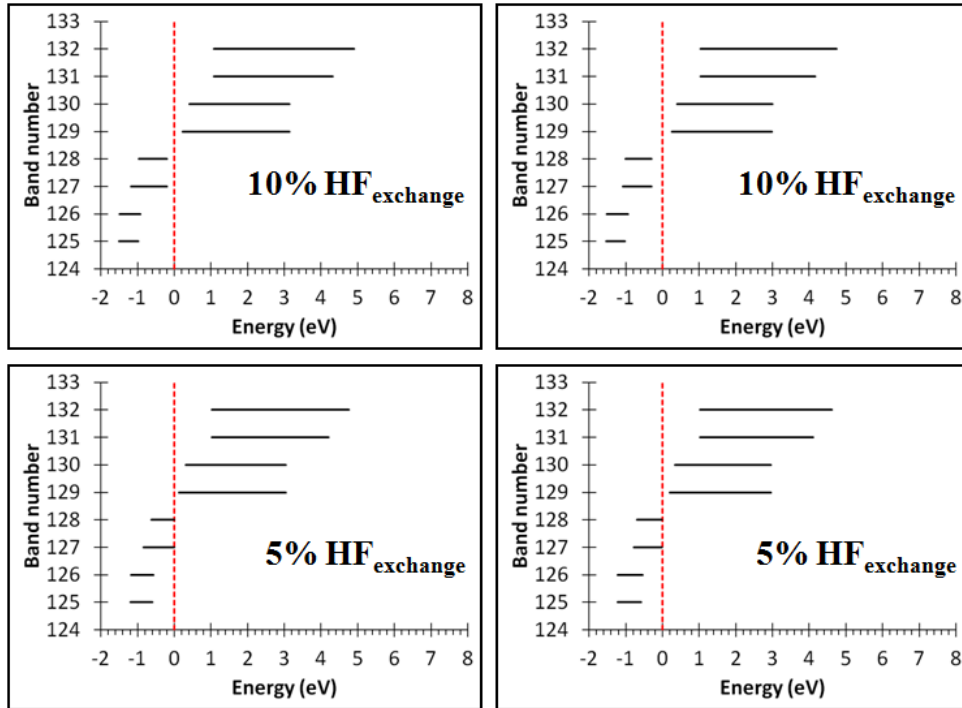


**Figure 2.8** Bandwidth for FeSb<sub>2</sub> at the experimental geometry evaluated with the PBE (left) and B3PW (right) functionals and considering different amount of %HF<sub>ex</sub> (Top: 10%; Bottom: 5%).

However, with respect to what already obtained with the original formulation of PBE and B3PW, no significant differences can be highlighted in how the atomic orbitals are combined to give the resulting bonding scheme (see next paragraph).

Finally, FeSb<sub>2</sub> has also been considered as the reference to evaluate the effects of an atoms description based on pseudo-potentials, in order to take into account relativistic effects not accounted for in the all-electron description. Whether they're not particularly important in this system or their effect is not affecting the features being considered, the final outcome is that even in this case no differences can be highlighted (Figure 2.9). Even the band gap dependency on the %HF<sub>ex</sub> value is as observed before (0.11eV and 0.13eV for PBE and B3PW, respectively, adopting %HF<sub>ex</sub> = 5).

In conclusion, concerning orbital-based analyses, almost indistinguishable results are obtained whether the theoretical or the experimental structure is adopted and for the different levels of

theory. In order to adopt the same level of theory for all the compounds while avoiding the wrong Fe-Sb bonding distances in optimized FeSb<sub>2</sub>, the results obtained from the experimental TZ/PBE description will be discussed in the next paragraph. However, the optimized TZ/PBE description for FeS<sub>2</sub> and FeP<sub>2</sub> will also be taken into account to provide a more direct comparison with the results obtained along a *gedanken* “reaction” from *M* to *L* for FeS<sub>2</sub>, for which optimized geometries were used.

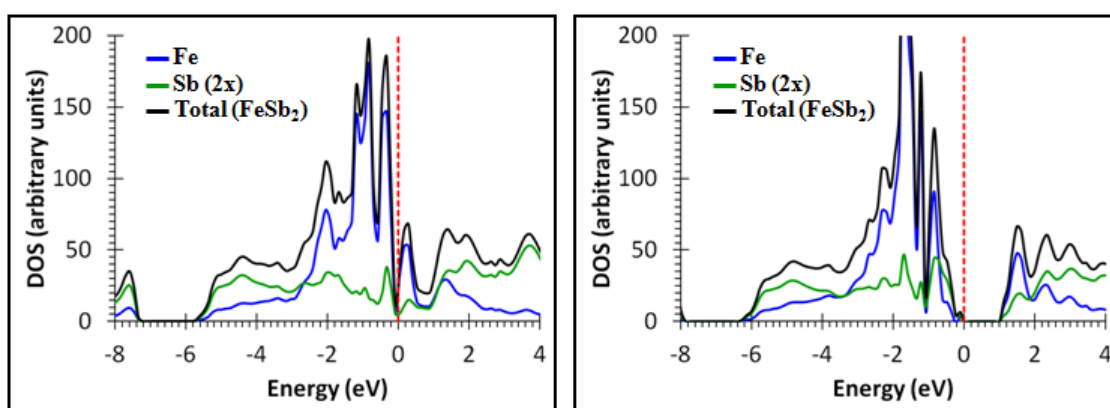


**Figure 2.9** Density Of States (DOS) for FeSb<sub>2</sub> the experimental geometry evaluated with the PBE (left) and B3PW (right) functionals (PP basis set). For each structure, the total and the atom-projected DOS (pDOS) are shown.

#### 4.2. Electronic structure: orbital-based analysis

Figure 2.10 introduces further detail by showing the contributions from individual Fe *d* orbitals to the DOS of FeS<sub>2</sub> and FeP<sub>2</sub>. The picture arising from these projected DOS for FeS<sub>2</sub> (Figure 2.10 left) is qualitatively consistent with the view that LFT has on the marcasitic distortion from the perfect octahedral field:  $d_{x^2-y^2}$  and  $d_{z^2}$  orbitals ( $e_g$ -like) give rise to bonding and antibonding states through combination with the S  $p_x$ ,  $p_y$  and  $p_z$  orbitals. Conversely,  $d_{xy}$ ,  $d_{xz}$  and  $d_{yz}$  ( $t_{2g}$ -like) behave as nonbonding orbitals, with  $d_{xy}$  slightly shifted to higher energies. It is thus possible to distinguish three regions in such orbital projected DOS (Figure 2.10). The first, denoted as *B*, is dominated by

the bonding interactions and it is peaked at  $\sim -4\text{eV}$  with respect to the FL at  $0\text{ eV}$ . The second, named as *AB* and peaked at  $\sim +2\text{eV}$ , is the anti-bonding counterpart, while the third, that we call *NB*, is dominated by nonbonding interactions and peaks at  $\sim -1\text{eV}$ . The small DOS that can be found in the *B* region due to the nonbonding orbitals, as well as the DOS attributed to  $d_{x^2-y^2}$  and  $d_{z^2}$  in the *NB* region, are likely to be caused by the marcasitic distortion.

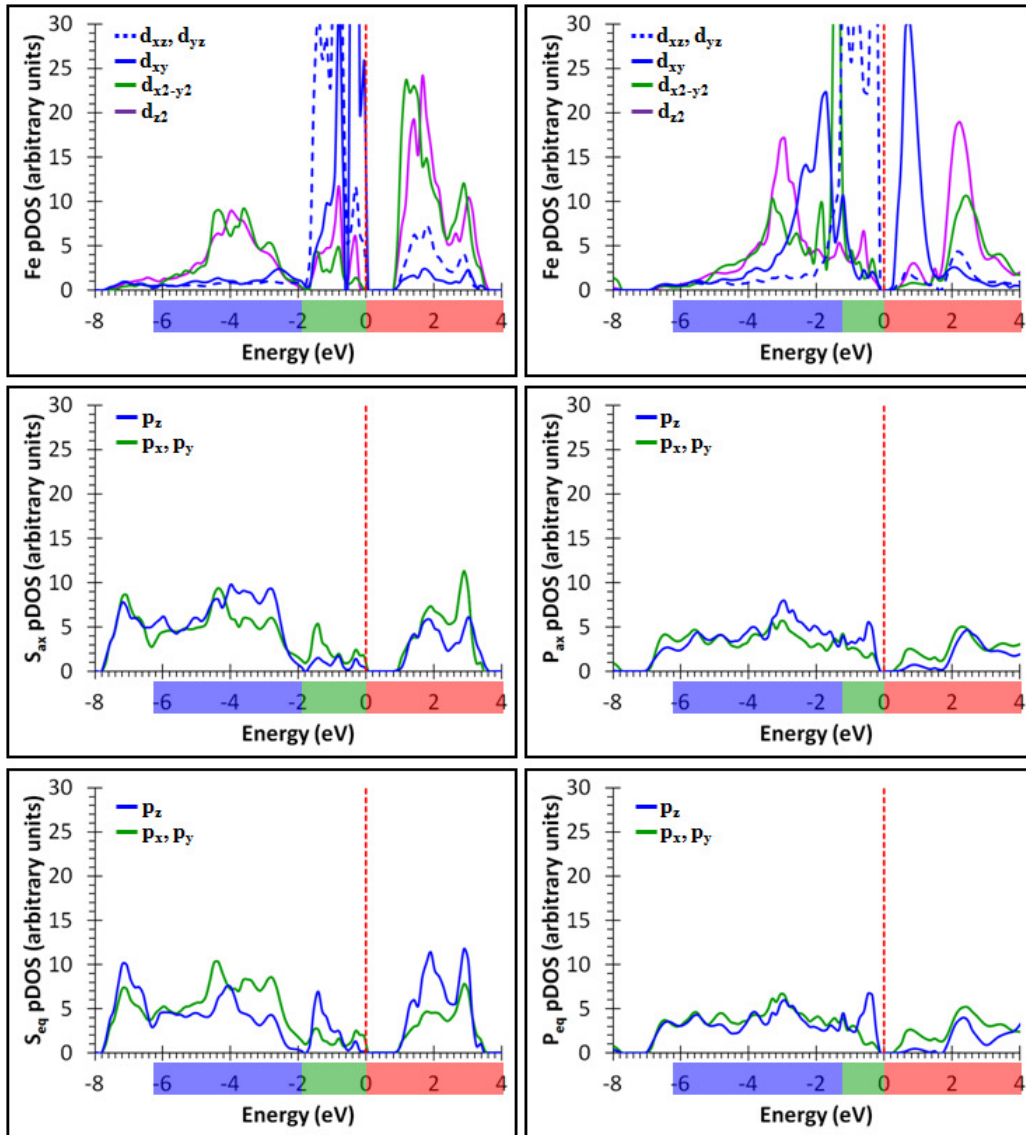


**Figure 2.10**  $\text{FeX}_2$  Individual Atomic Orbitals projected DOS (pDOS) for the optimized  $\text{FeS}_2$  (left) and  $\text{FeP}_2$  (right) structures. Fe  $d$  orbital states (top); X  $p$  orbital states: X-axial (middle) and X-equatorial (bottom). The blue, red and green boxes on the abscissa highlight the Bonding (*B*), Anti-Bonding (*AB*) and Non Bonding (*NB*) energy regions, respectively (see text).

Mulliken orbital populations (Table 2.6) condense the information from the projected DOSs into numeric population values for each orbital and take implicitly into account the position of the FL (orbital contributions are integrated up to the FL). These population values necessarily comply with the qualitative picture sketched above while providing quantitative detail. The  $t_{2g}$ -like states have a larger population than the  $e_g$ -like orbitals, though still far from two, which is the value one would expect from a fully ionic picture ( $\text{Fe}^{+2}$ ) and from their ideal “non bonding” nature. The  $e_g$ -like orbitals are found to be mostly half-filled instead of being empty as required by the LFT. According to the Mulliken analysis, the resulting total  $d$ -population on Fe is  $6.78 e^-$ , a value in between a purely covalent and a purely ionic picture.

**Table 2.6** Fe  $3d$  orbitals’ Mulliken populations for the experimental  $\text{FeX}_2$  ( $X=\text{S, P, As, Sb}$ ) structures.

Fe $3d$ orbital	$\text{FeS}_2$	$\text{FeP}_2$	$\text{FeAs}_2$	$\text{FeSb}_2$
$yz$	1.61	1.64	1.64	1.64
$xz$	1.61	1.64	1.64	1.64
$xy$	1.77	1.13	1.13	1.13
$x^2-y^2$	0.85	1.30	1.32	1.34
$z^2$	0.95	1.09	1.09	1.13

The  $B$ ,  $AB$  and  $NB$  regions can also be identified for  $\text{FeP}_2$  (Figure 2.10 right). However, at variance with  $\text{FeS}_2$ , the  $d_{xy}$  orbital in  $\text{FeP}_2$  no longer contributes in the  $NB$  region, while it does so in both the  $B$  and  $AB$  regions. According to the fully ionic picture,<sup>12</sup> two more electrons ( $\text{Fe}^{+4}$ ) are withdrawn from iron in  $\text{FeP}_2$ , with the  $d_{xy}$  orbital being emptied and raised above the Fermi level. In reality, the population of the  $d_{xy}$  orbital ( $1.13 e^-$ , Table 2.6) is indeed highly decreased with respect to that in  $\text{FeS}_2$  ( $1.77 e^-$ , Table 2.6), however, its value close to one indicates that this orbital is involved in bonding (figure 10 right) and that it is contributing to the DOSs both below and above the FL. At variance with the ionic picture, the total Mulliken population of the iron  $d$  orbitals remains almost unchanged ( $6.80 e^-$ ) to the value it has in  $\text{FeS}_2$ . The almost constancy in the  $d$  orbitals population is

the result of the mentioned decrease of the  $d_{xy}$  population (from 1.77 to 1.13  $e^-$ ) being almost compensated for by a significant increase of the  $d_{x^2-y^2}$  population (from 0.85 to 1.30  $e^-$ ). In  $\text{FeP}_2$  both  $d_{x^2-y^2}$  and  $d_{xy}$  become involved in the bonding in the equatorial plane, but the two orbitals exchange their roles with respect to  $\text{FeS}_2$ :  $d_{x^2-y^2}$  tends to become non bonding, while  $d_{xy}$  acquires a significant bonding character. This view becomes particularly clear and it is rigorously proven when bonding analysis is performed in terms of observables (see next paragraph).

The question arises whether the observed change in the electronic structure of iron is primarily the result of the compression along  $c$  on going from  $M$  to  $L$  or is rather due to the reduction of two valence electrons when the 16-group replace the 15-group elements in  $\text{TX}_2$ . To elucidate this point, an imaginary “reaction” from  $M$  to  $L$  for  $\text{FeS}_2$  has been considered, by retaining the  $Pnmm$  space group and taking the optimized  $\text{FeS}_2$  and  $\text{FeP}_2$  unit cells as the starting and final points of such transformation. The lattice parameters of three intermediate structures  $S1$ ,  $S2$  and  $S3$  (Table 2.7) have been obtained as equidistant points of a linear variation of the cell edge values along the  $M$  to  $L$  reaction path. The fractional coordinates in Table 2.7 are the result of the supposed linear variation of Fe-X distances along the transformation. Since  $\text{FeS}_2$  and  $\text{FeP}_2$  have an equal ratio of the axial to the equatorial Fe-X distances, the ratio of such distances remains automatically constant (Table 2.7) along the reaction path. Differently from the changes observed between  $\text{FeS}_2$  and  $\text{FeP}_2$ , the  $d$ -orbital populations (Table 2.7) are marginally affected by the only geometrical variation considered in the  $\text{FeS}_2$   $M$  to  $L$  transformation. Moreover changes take place almost only during the last step of the transformations (i.e. from  $S3$  to  $L$ ). Though much smaller, the observed changes are qualitatively similar to those found between  $\text{FeS}_2$  and  $\text{FeP}_2$ , with the population of  $d_{x^2-y^2}$  increasing from 0.86 to 1.02  $e^-$  and that of  $d_{xy}$  decreasing from 1.77 to 1.66  $e^-$ . The total electron  $d$ -population remains almost unchanged, around to  $6.81 \pm 0.3 e^-$  along the whole reaction path.

**Table 2.7** FeS<sub>2</sub> marcasite (*M*) to löllingite (*L*) transformation. S1, S2 and S3 are the intermediate structures obtained as equidistant points of a linear variation of the cell edge values along the *M* to *L* reaction path. Lattice parameters *a*, *b*, and *c* are given in Ångstrom; *x* and *y* are the fractional coordinates of the S atom; *ax.* and *eq.* identify the Fe-S equatorial and axial interactions and their bond lengths are given in Ångstrom;  $\alpha$ , given in degrees, is the X-Fe-X “compression” angle;  $P_{Mull}$  are the Mulliken’s populations for the various Fe 3*d* orbitals.

	<i>M</i>	<i>S1</i>	<i>S2</i>	<i>S3</i>	<i>L</i>
<i>a</i> (Å)	4.4426	4.5759	4.7092	4.8425	4.9758
<i>b</i> (Å)	5.4114	5.4717	5.5321	5.5925	5.6529
<i>c</i> (Å)	3.3956	3.2275	3.0594	2.8914	2.7233
<i>x</i>	0.2051	0.1913	0.1813	0.1748	0.1703
<i>y</i>	0.3763	0.3757	0.3740	0.3711	0.3676
Fe-S ax. (Å)	2.2311	2.2343	2.2382	2.2414	2.2444
Fe-S eq. (Å)	2.2464	2.2499	2.2535	2.2560	2.2594
$\delta$ (°)	98.2	91.7	85.5	79.7	74.1
$P_{Mull}$ (Fe- <i>d</i> <sub>yz</sub> )	1.60	1.60	1.60	1.58	1.57
$P_{Mull}$ (Fe- <i>d</i> <sub>xz</sub> )	1.60	1.60	1.60	1.58	1.57
$P_{Mull}$ (Fe- <i>d</i> <sub>xy</sub> )	1.77	1.78	1.78	1.74	1.66
$P_{Mull}$ (Fe- <i>d</i> <sub>x<sup>2</sup>-y<sup>2</sup></sub> )	0.86	0.86	0.88	0.94	1.02
$P_{Mull}$ (Fe- <i>d</i> <sub>z<sup>2</sup></sub> )	0.97	0.96	0.96	0.98	1.02

It is worth noting that the DOSs portraits displayed in Figure 2.11 reveal a qualitative difference between the *M* and *L* electron structures of FeS<sub>2</sub> which was hidden in the analysis of the *d*-orbital population: while the *d*<sub>x<sup>2</sup>-y<sup>2</sup></sub> and *d*<sub>xy</sub> contributions show only a marginal overlap below the Fermi level in the *M* structure, they share instead a similar energy range in the *L* geometry, denoting an initial tendency to be more similarly involved in bonding. However, such tendency realizes in practice only when S is substituted for P.

### 4.3. Electronic structure: observable-based analysis

According to the QTAIM theory,<sup>29</sup> the structure of a compound can be revealed through the topological analysis of  $\rho$  by studying its critical points (cps); in particular those cps called bond critical points (bcps) which tell us how atoms get bonded to one another.

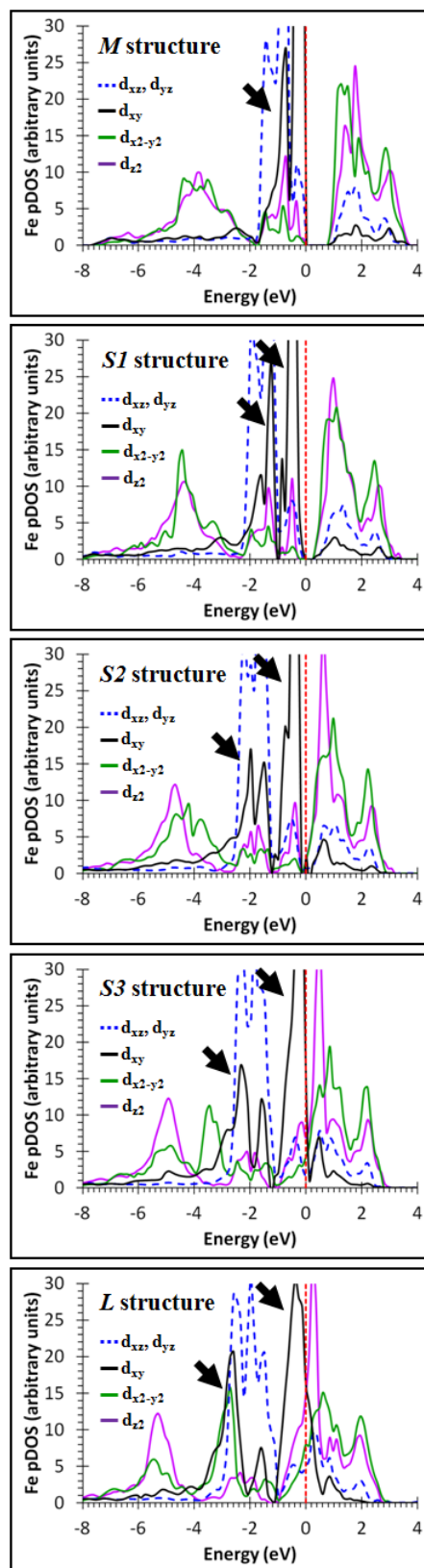


**Figure 2.11** Individual Atomic Orbitals projected DOS (pDOS) of the Fe  $d$  orbital states in the  $M$ ,  $S1$ ,  $S2$ ,  $S3$  and  $L$  structures of  $\text{FeS}_2$  (from top to bottom). The black arrows highlight the splitting of the  $d_{xy}$  orbital.

At bcps, the electron density attains its minimum value along the bond path, the line of maximum electron density with respect to any arbitrary displacement which links the two bonded atoms.<sup>29</sup> For each of the studied systems, either considering the experimental or theoretical structures, the same number, type and Wyckoff position of cps were found. Three bcps were identified, B1, B2 and B3, related respectively to the axial and equatorial Fe-X interaction, and to the short X-X interaction ( $X = S$ : 2.154Å;  $X = P$ : 2.2365Å;  $X = As$ : 2.4915Å,  $X = Sb$ : 2.8941Å) (Figure 2.12).

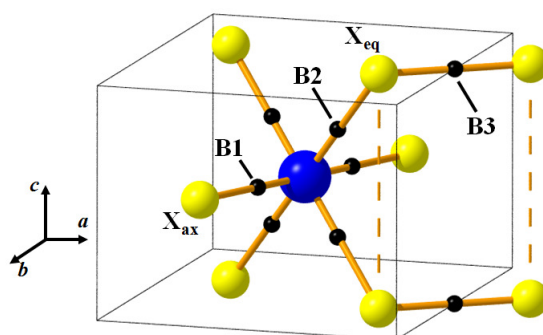


**Figure 2.12** B1, B2 and B3 type bond critical points (bcps) in  $FeX_2$ . Fe atom is represented by a blue sphere, X atoms by yellow and bcps by small black spheres. Two  $X_2$  dumbbells have also been added to highlight the presence of an interaction (B3 bcp) between the atoms constituting the dumbbell but not between the atoms of different dumbbells (dashed lines).

It is worth noting that no bcp, hence no direct  $X \cdots X$  interaction ( $X = S$ : 3.3871Å;  $X = P$ : 2.7230Å;  $X = As$ : 2.8822Å,  $X = Sb$ : 3.19733Å), was found between the diatomic anions ( $X_2$ ) in the direction along  $c$  (Figure 2.12), although Papoian and Hoffmann<sup>14</sup> have hypothesized its occurrence to fulfill the 18-electron counting rule in  $FeSb_2$ . As for what concerns the topological parameters at the various cps (Table 2.8), few differences can be highlighted between the experimental and the optimized structures, the only one worth mentioning being the change in sign of the Laplacian,  $\nabla^2\rho$ , for the S-S bcp.

**Table 2.8**  $\text{FeX}_2$  ( $\text{X}=\text{S},\text{P}$ ) bcp properties for the experimental (exp.) and optimized (opt.) structures. B1, B2 and B3 denotes the axial, the equatorial Fe-X interaction, and the short X-X interaction, respectively;  $d_{\text{Fe-X}}$  and  $d_{\text{X-X}}$  are the Fe-X and X-X distances (in Ångstrom); AIL is the Atomic Interaction Line<sup>29</sup> (called bond path at equilibrium) and  $\text{AIL}_{\text{X-bcp}}$  ( $\text{AIL}_{\text{Fe-bcp}}$ ) are the distances from X (Fe) atom to bcp, on moving along the AIL;  $\rho$  and  $\nabla^2\rho$  are the electron density and the Laplacian of the electron density at the bcp, in  $\text{e}/\text{Å}^3$  and  $\text{e}/\text{Å}^5$  respectively;  $\varepsilon$  is the ellipticity at the bcp. The values in parentheses refer to the optimized structures.

	FeS2	FeP2	FeAs2	FeSb2	
B1	$d_{\text{Fe-X}}$ (Å)	2.2359 (2.2311)	2.2484 (2.2444)	2.3620 (2.3625)	2.5746 (2.6216)
	$\text{AIL}_{\text{Fe-bcp}}$ (Å)	1.0095 (1.0092)	1.0503 (1.0495)	1.0864 (1.0873)	1.1702 (1.1811)
	$\text{AIL}_{\text{X-bcp}}$ (Å)	1.2266 (1.2220)	1.1982 (1.1951)	1.2759 (1.2755)	1.4049 (1.4409)
	$\rho$ ( $\text{e}/\text{Å}^3$ )	0.568 (0.575)	0.592 (0.596)	0.507 (0.507)	0.415 (0.387)
	$\nabla^2\rho$ ( $\text{e}/\text{Å}^5$ )	5.151 (5.117)	2.767 (2.792)	2.320 (2.300)	1.226 (1.185)
	$\varepsilon$	0.034 (0.032)	0.009 (0.004)	0.002 (0.001)	0.024 (0.027)
	B2	$d_{\text{Fe-X}}$ (Å)	2.2539 (2.2464)	2.2637 (2.2594)	2.3874 (2.3813)
$\text{AIL}_{\text{Fe-bcp}}$ (Å)		1.0201 (1.0187)	1.0881 (1.0872)	1.1299 (1.1279)	1.2129 (1.2098)
$\text{AIL}_{\text{X-bcp}}$ (Å)		1.2423 (1.2363)	1.1764 (1.1729)	1.2580 (1.2539)	1.3848 (1.3825)
$\rho$ ( $\text{e}/\text{Å}^3$ )		0.548 (0.558)	0.563 (0.567)	0.478 (0.483)	0.388 (0.390)
$\nabla^2\rho$ ( $\text{e}/\text{Å}^5$ )		5.012 (5.030)	1.928 (1.918)	1.718 (1.728)	0.995 (1.042)
$\varepsilon$		0.011 (0.007)	0.024 (0.024)	0.034 (0.034)	0.075 (0.056)
B3		$d_{\text{X-X}}$ (Å)	2.2154 (2.2613)	2.2365 (2.2610)	2.4915 (2.5135)
	$\text{AIL}_{\text{X-bcp}}$ (Å)	1.1077 (1.1307)	1.1184 (1.1307)	1.2458 (1.2568)	1.4471 (1.4466)
	$\rho$ ( $\text{e}/\text{Å}^3$ )	0.743 (0.687)	0.742 (0.714)	0.529 (0.512)	0.371 (0.372)
	$\nabla^2\rho$ ( $\text{e}/\text{Å}^5$ )	-0.256 (0.109)	-2.735 (-2.438)	-0.543 (-0.453)	-0.170 (-0.184)
	$\varepsilon$	0.032 (0.029)	0.022 (0.022)	0.008 (0.008)	0.012 (0.002)

By optimizing the geometry, the S-S bond lengthens and the Laplacian becomes slightly positive instead of being negative and very close to zero as in the experimental geometry structure. However, although positive ( $0.109 \text{ e}\text{\AA}^{-5}$ ), it is much less so than the value ( $2.588 \text{ e}\text{\AA}^{-5}$ , Table 2.9) one would obtain by placing two non interacting S atoms at the same internuclear distance (Fig. 2.13). This observation implies that the S-S interaction, compared to the non-bonding case, maintains a (tendency to a) shared-shell (*covalent*) bond nature even in the optimized structure despite the Laplacian being positive at the bcp.

**Table 2.9**  $\text{FeX}_2$  (X=S,P) : Laplacian values at the X-X bcp in the crystal and those in the free atom X, multiplied by two, at the bcp distance from the nucleus in the crystal.  $\Delta\nabla^2\rho$  are the differences between  $\nabla^2\rho$  values at X-X bcp in the crystal (at optimized or experimental geometry) and those, multiplied by two, in the free atom X at the bcp distance from the nucleus in the crystal.

	$\nabla^2\rho$ ( $\text{e}/\text{\AA}^5$ )			$\Delta\nabla^2\rho$ ( $\text{e}/\text{\AA}^5$ )	
	crystal (exp)	crystal (opt)	free atom (2x)	exp	opt
S-S	-0.256	0.109	2.588	-2.844	-2.479
P-P	-2.735	-2.438	1.050	-3.785	-3.488

As for what concerns the Fe-X interactions,  $\nabla^2\rho$  is found to be positive in all cases. The bcp is located at about  $1 \text{ \AA}$  from the iron and at about  $1.2 \text{ \AA}$  from the S or P atoms, that is at distances which fully fall (Figure 2.13) in the depletion region of the M quantum shell of all these atoms when isolated (and neutral).

The resulting positive Laplacian at the bcp is therefore not surprising, the observed values being about 5 and 7% (ax, eq, respectively;  $\text{FeS}_2$ ) and 26 and 37% (ax, eq, respectively;  $\text{FeP}_2$ ) smaller than the sum of the isolated atom contributions. The higher percentage decrease found for  $\text{FeP}_2$  is likely a sign of an enhanced covalency in this compound with respect to  $\text{FeS}_2$ . Such finding is also corroborated by the smaller Bader net charge found on iron for  $\text{FeP}_2$  ( $+0.25e^-$  rather than  $+0.67e^-$  in  $\text{FeS}_2$ , Table 2.10).

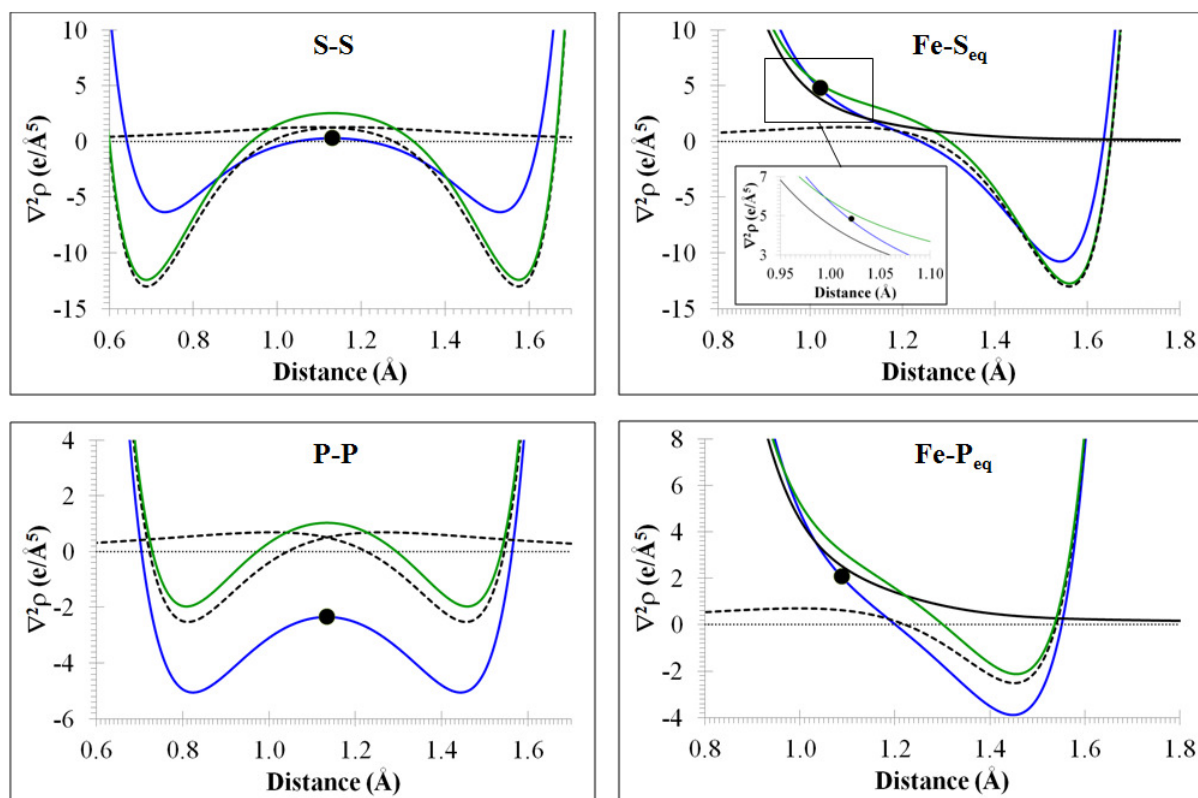


**Figure 2.13** Laplacian profiles along the X-X (top left: X = S; bottom left: X = P; one atom is placed at the origin) and Fe-X<sub>eq</sub> (top right: X = S; bottom right: X = P; the Fe atom is placed at the origin) interaction lines. The profiles portrayed refers to the crystal (solid blue), to the isolated atoms (Fe: solid black; X: dashed black) and to the sum of the isolated atoms (solid green) Laplacian densities. The black dots mark the position of the bond critical point (bcp) in the crystal. On the x axes is reported the distance from the origin.

**Table 2.10** Bader's electron populations,  $N(\Omega)$ , and net charges,  $q(\Omega)$  for the experimental structures.

Atom $\Omega$		FeS <sub>2</sub>	FeP <sub>2</sub>	FeAs <sub>2</sub>	FeSb <sub>2</sub>
Fe	$N(\Omega)$	25.33	25.75	25.85	26.17
	$q(\Omega)$	0.67	0.25	0.15	-0.17
X	$N(\Omega)$	16.33	15.13	33.07	50.91
	$q(\Omega)$	-0.33	-0.13	-0.07	+0.09

The small departure of the bcp density from that found with the non-interacting model is in line with a dative bonding description for FeS<sub>2</sub>. Indeed, the electron density at the Fe-X bcp is as much

as 20% smaller than the sum of the isolated atom densities in FeS<sub>2</sub>, whereas, in FeP<sub>2</sub>, in agreement with the enhanced shared character of the Fe-X interaction, it is larger than this sum by about 1-4%. Further interesting insight into the relationships between *d*-orbital populations, metal-ligand interactions and formal number of electrons on the metal in the studied compounds is obtained by considering the Laplacian density topology.<sup>29</sup> As it has been repeatedly shown in a number of papers,<sup>30,31,32,33,34</sup> the Laplacian distribution reflects the deviation from spherical symmetry which results from an incomplete filling of the valence shell orbitals of an atom. By combining a study of the Laplacian topology with an orbital-based analysis, light is shed on the correspondence between the portrait of an observable in a given system and the expectations of the orbital model and of the LFT in an idealized representation of this same system.<sup>30,31,32</sup> In a perfect octahedral field, the total *t<sub>2g</sub>* orbital electron density has eight lobes pointing along the diagonal of a cube while the density associated with the *e<sub>g</sub>* orbitals has six lobes pointing towards the faces of a cube.<sup>35</sup> If the *t<sub>2g</sub>* orbitals are filled and the *e<sub>g</sub>* are empty, as it occurs in the Cr (*t<sub>2g</sub>*)<sup>6</sup> configuration,<sup>31</sup> the resulting Laplacian distribution has a cubic shape with density accumulations along the diagonals of the cubes and holes(depletions) at the center of the faces. It has also been shown<sup>36,37</sup> that the donor-acceptor interaction between a metal atom and the surrounding ligands may be often interpreted in terms of a so-called 'key-lock' mechanism, where a  $-\nabla^2\rho$  lump on the ligand is aligned to, and matches with, a  $-\nabla^2\rho$  hole on the metal. This for instance occurs<sup>31</sup> in the case of the prototypical Cr(CO)<sub>6</sub> metal-ligand complex whose key-lock arrangement of charge concentrations and depletions is opposite to the one usually found for AY<sub>n</sub> complexes,<sup>33</sup> in which A is a main group element. In this latter case, the charge concentrations in the Valence Shell Charge Concentration (VSCC)<sup>37</sup> region of A are directed towards the ligands and neither lie in-between two neighboring ligands nor are oppositely located (LOCC, Ligand-Opposed Charge Concentrations).<sup>33</sup> These two contrasting mechanisms denote the limiting situations of bonding in the two cases, a closed-shell dative interaction for

Cr(CO)<sub>6</sub> and a shared-shell, covalent or covalent-polar interaction for AY<sub>n</sub>. Our systems differ from Cr(CO)<sub>6</sub> under many aspects. First, a distortion from perfect octahedral symmetry occurs, which leads to partial filling of all orbitals even for a *d*-electron population on the metal lower than six. Secondly, the number of *d*-electrons on the metal is not exactly six and its estimated value depends on the adopted model or on the chosen charge partitioning scheme. We already noted that in the fully ionic model such value amounts to six for FeS<sub>2</sub> and four for FeP<sub>2</sub>, while we found it to be equal to 6.94 e<sup>-</sup> and 6.92 e<sup>-</sup>, respectively, in the Mulliken's approach and to 7.33 e<sup>-</sup> and 7.74 e<sup>-</sup> according to Bader's partitioning.<sup>b</sup> Finally, the dative and covalent bonding schemes enter in competition in these systems, with the second scheme largely enhancing its weight in FeP<sub>2</sub> compared to FeS<sub>2</sub>.

In the ∇<sup>2</sup>ρ contour maps for FeS<sub>2</sub> (Figure 14 left, top and middle), a *t*<sub>2g</sub><sup>6</sup>-like octahedral VSCC can be recognized for the iron atom, with the regions of charge depletion (or, more precisely, of less charge accumulation)<sup>c</sup> being approximately aligned to the S regions of charge accumulation in a pseudo key-lock structure.<sup>31</sup> This is made clear in Fig. 2.15 left (top and in particular bottom) where one notices that the -∇<sup>2</sup>ρ maxima on Fe bisect the angles formed by the -∇<sup>2</sup>ρ maxima on S pointing towards the iron nucleus and this same nucleus as central vertex of these angles. A closer exam of Figure 2.14 (left, middle) and Fig. 2.14 (left, bottom) reveals, however, that in the equatorial plane a slight but noticeable misalignment of the charge concentration with respect to the charge depletion regions also occurs. This can easily be explained by the geometrical distortions occurring in this

---

<sup>b</sup> In the case of Bader's partitioning, individual orbital populations are not defined. The given estimate of *d* orbital population, according to this partition, assumes that the iron atom has a frozen Ar core and that its 4s<sup>2</sup> electrons have been entirely transferred to the ligands.

<sup>c</sup> With respect to the ideal *t*<sub>2g</sub><sup>6</sup> octahedral case, the regions associated with the e<sub>g</sub> orbital densities, rather than being regions of charge depletion, are, for our systems, regions of decreased charge concentration only. As we said before, the population of the Fe *d* orbitals exceeds 6 e<sup>-</sup> in FeS<sub>2</sub> (and FeP<sub>2</sub>) and the geometrical arrangement of the ligands around the Fe differs from the ideal octahedral case. Both these facts have an impact on the distribution of *d* electrons density around the Fe atom and hence on the portrait of the total ∇<sup>2</sup>ρ distribution.

plane (the  $\delta$  angle significantly deviates from  $90^\circ$ , Table 2.2) and, quite interestingly, also in terms of the known relationships between the properties of the VSCC and the VSEPR model.<sup>38,37</sup> Namely, the S charge concentrations directed towards the Fe atom rotate in the equatorial plane so as to diminish their overlap with the neighboring concentration associated to the smaller S-Fe-S' angle ( $180^\circ - \delta$ , see Table 2.2). In such a way, the repulsion between the charge concentrations of the closer neighboring pairs of S atoms is decreased, while that of the farther neighboring pairs is enhanced, making these repulsions more alike to each other.

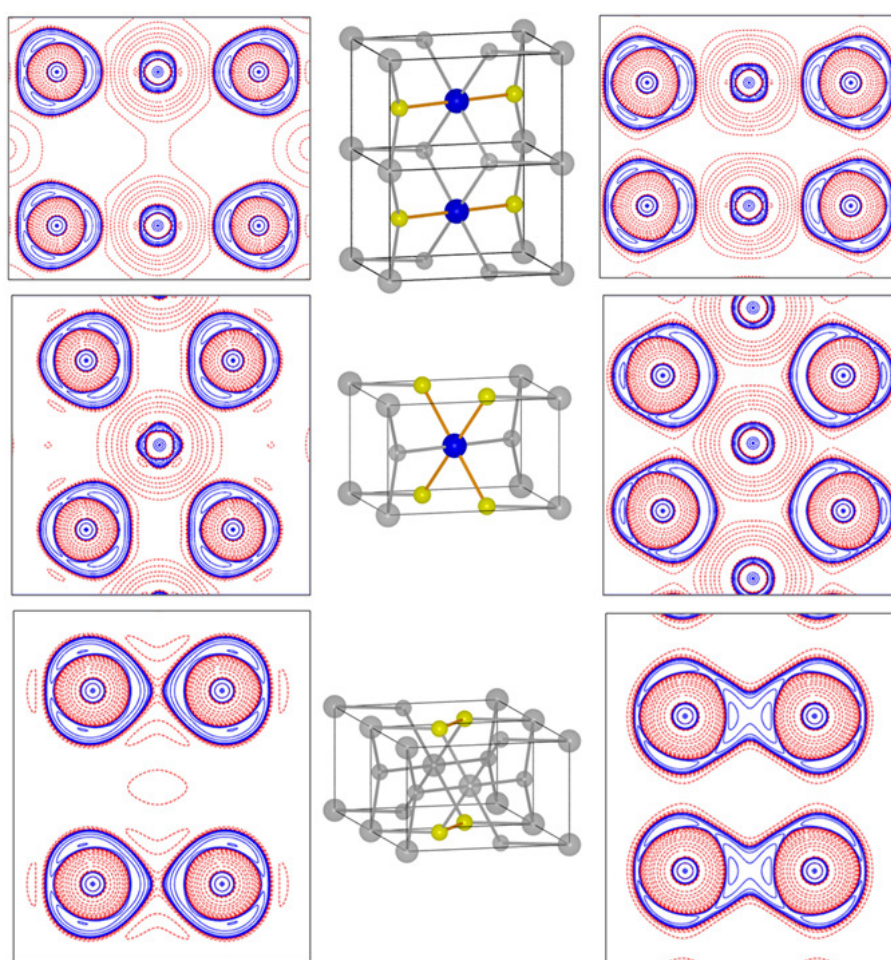


**Figure 2.14**  $\nabla^2\rho$  maps for the optimized  $\text{FeS}_2$  (left) and  $\text{FeP}_2$  (right) structures. Solid blue line mark regions of charge accumulation (negative  $\nabla^2\rho$ ) while dotted red lines mark regions of charge depletion (positive  $\nabla^2\rho$ ). For each structure, the plane defined by the axial Fe-X (top), equatorial Fe-X (middle) and X-X (bottom) interactions is shown. The pictures in the middle identify the considered planes.

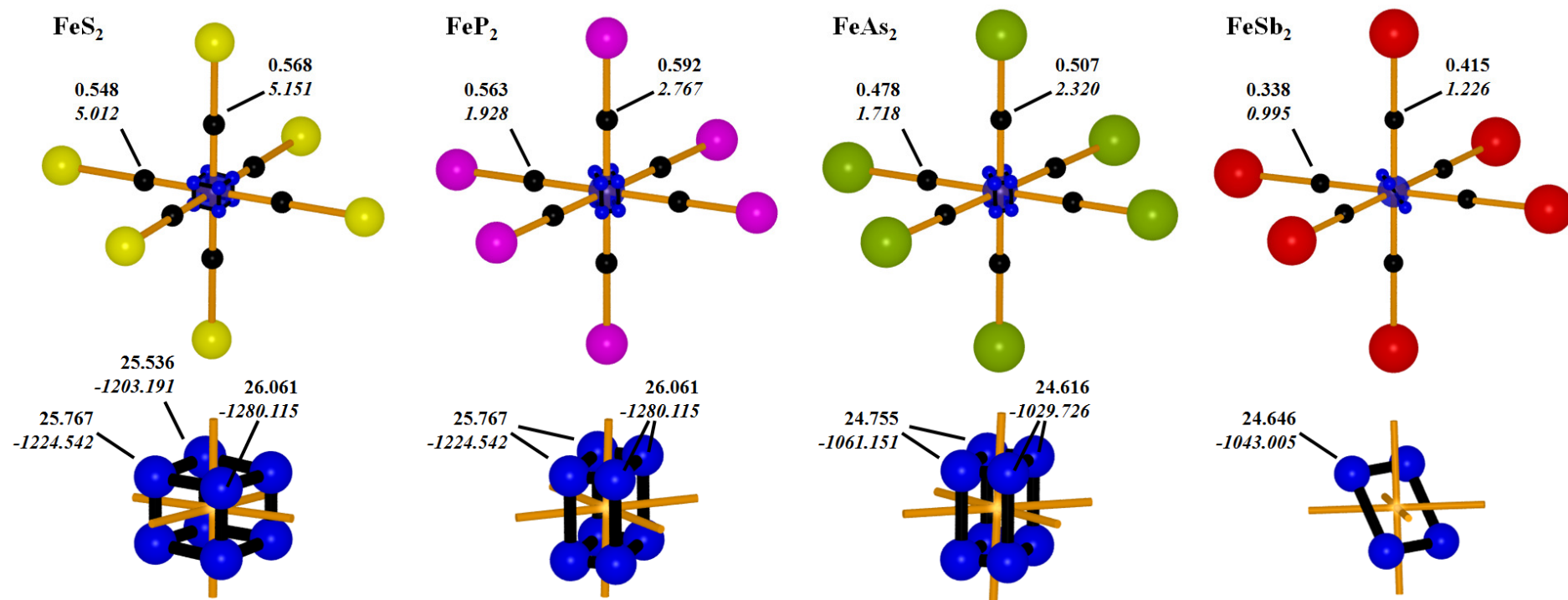


**Figure 2.15**  $\nabla^2\rho$  topology around the Fe atom and along the Fe-X interactions for the experimental structures. The large blue, yellow, purple, green and red spheres represent the Fe, S, P, As and Sb atoms respectively. The small black spheres mark the position of the bcp while the small blue spheres define the position of the  $\nabla^2\rho$  minima (region of charge accumulation) found within Fe and VSCC. The inset shows an enlargement of the charge accumulations spatial distribution. The values of  $\rho$  (in  $\text{e}/\text{\AA}^3$ ) and  $\nabla^2\rho$  (in  $\text{e}/\text{\AA}^5$ ) for the bcp and  $\nabla^2\rho$  minima are reported in normal and italics respectively.

The misalignment of the S concentrations with respect to the (S-Fe)<sub>eq</sub> axis is further evidenced in Figure 2.16, which shows the four  $-\nabla^2\rho$  VSCC maxima around each S atom. Their location nicely complies with a  $sp^3$ -like hybridization of S. The mentioned misalignment enables those two concentrations of S pointing towards two equatorial iron atoms not only to stay further apart than implied by the Fe<sub>eq</sub>-S-Fe<sub>eq</sub> angle (97.94°, equal to the S-Fe-S  $\delta$  angle, Table 2.2 and Figure 2.3), but to even surpass the  $sp^3$  tetrahedral value by about six degree (115.4°). In such a way, the distance and the repulsion among the charge concentrations involved in the dative-like bonds (those with more “lone-pair”, or more precisely, non-shared pair character)<sup>d</sup> are, respectively, maximized and minimized. Likewise, also the two S charge concentrations pointing towards an equatorial and an axial Fe atom, though slightly decreasing their angle with respect to the Fe<sub>eq</sub>SFe<sub>ax</sub> angle, still retain an angle of 117.1°, significantly larger than the tetrahedral value. Instead, any pair of S concentrations pointing toward the bonded sulphur atom S' and either one axial or one equatorial Fe atom form a much narrower FeSS' angle of about 101°, since the S charge concentration directed towards S' has more a bonding rather than a lone-pair like character. In conclusion, the misalignment of the S charge concentrations with the relative charge depletions on Fe has clearly a twofold origin. On one hand it allows an equalization of the repulsion between lone-pair like concentrations of different S atoms (Figure 2.14 left, middle and Figure 2.15, left) and on the other hand it enables the minimization of the repulsion between the lone-pair like concentrations on each S atom (Figure 2.16 left).

---

<sup>d</sup> Clearly, when referring to bonding or lone-pair (“non-shared” pair) character of the charge concentrations, it is not to be intended that their associated regions will include a full electron pair: it simply refers to the more or less shared nature of the fraction of an electron pair enclosed in that region.

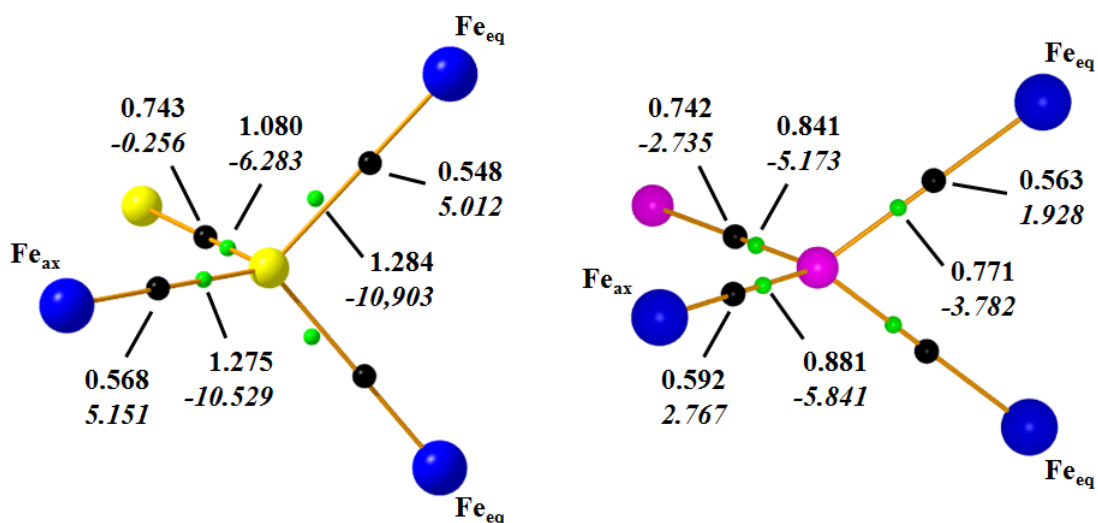


**Figure 2.16**  $\nabla^2\rho$  topology of the X atom for the optimized FeS<sub>2</sub> (left) and FeP<sub>2</sub> (right) structures. The large blue, yellow and purple spheres represent the Fe, S and P atoms respectively. The small black spheres mark the position of the bcp while the small green spheres define the position of the  $\nabla^2\rho$  minima (region of charge accumulation) found within X VSCC respectively. The values of  $\rho$  (in e/Å<sup>3</sup>) and of  $\nabla^2\rho$  (in e/Å<sup>5</sup>) at bcp and at  $-\nabla^2\rho$  maxima are reported in normal and italics respectively.

We discuss now the FeP<sub>2</sub> system. In the  $\nabla^2\rho$  contour maps for FeP<sub>2</sub> (Figure 2.10 right, top and middle), the  $t_{2g}^6$ -like octahedral VSCC is hardly recognized for the iron atom, as opposed to what is the case for FeS<sub>2</sub>. The regions of charge depletion and charge accumulation are now very marginally differentiated, especially so in the plane of the equatorial (Figure 2.15) Fe-P bonds. In summary, the key-lock pattern of charge concentrations and depletions, typical of metal-ligand interactions, seems to be lost. Although the close exam of the  $-\nabla^2\rho$  topology around Fe still reveals the presence of eight charge concentrations, the Laplacian distribution has no longer an almost regular cubic shape, but has acquired that of a cuboid (Figure 2.15) with one side almost half as long, 0.24 Å, than the other two sides, 0.42 Å (for the sake of comparison the corresponding figures in FeS<sub>2</sub> are 0.32 and 0.38 Å)

As a consequence, the Fe charge concentrations approach each other in pairs (Figure 2.15) and, rather than bisecting, from above and below, the P<sub>eq</sub>-Fe-P<sub>eq</sub> angles, result almost aligned, from

above and below, to the Fe-P<sub>eq</sub> bonds (Figure 2.15). This bonding situation approaches that usually found for AY<sub>n</sub> complexes where A is a main group element. This is in nice compliance with the increased covalent character found for the Fe-X interaction when P substitutes S. The change in the Laplacian distribution around the iron atom also agrees with the observed decrease of the  $d_{xy}$  and parallel increase of the  $d_{x^2-y^2}$  (and also  $d_{z^2}$ ) population on moving from X=S to X=P (see previous paragraph). It is worth noting that the observed rotation of the iron VSCC maxima with respect to the ligands is primarily due to the different electronic nature of the S and P “ligands”, rather than a result of the change of geometry from *M* to *L* structure. Indeed, when FeS<sub>2</sub> with the *L* structure is considered, the location of the eight VSCC maxima of iron turns out hardly to be affected, despite noticeable changes in the values of  $\rho$  and  $\nabla^2\rho$  at such maxima.

For FeP<sub>2</sub>, the shared shell character of the P-P interaction is clearly visible (Figure 2.14 right bottom) and, at variance with FeS<sub>2</sub>, the separate charge concentration maxima on P pointing towards the iron atoms in the equatorial plane seem to have merged into a single maximum (Figure 2.14 right middle). A closer exam of the topology of  $-\nabla^2\rho$  shows that it is however still possible to distinguish four maxima also for FeP<sub>2</sub> though largely flattened (Figure 2.16, right) with respect to FeS<sub>2</sub>. Despite the fact that the Fe<sub>eq</sub>XFe<sub>eq</sub> angle is highly narrowed from 97.9° for X=S to a value of only 73.8° degrees for X=P, the charge concentrations pointing toward Fe<sub>eq</sub> are aligned along the Fe-P axes. There are two concurring reasons for such a behavior. Due to their increased bonding-nature, the charge concentrations in FeP<sub>2</sub> are no longer forced to stay as far apart as possible as it occurs in FeS<sub>2</sub>, despite the very small Fe<sub>eq</sub>PFe<sub>eq</sub> angle. The enhanced bonding character of such concentrations is also revealed by their largely increased proximity to the B2 bcp, 0.36 Å, to be compared to a value of 0.55 Å in FeS<sub>2</sub>. A second clear rationale of why the two VSCC maxima on the P atoms pointing towards the Fe<sub>eq</sub> atoms get closer and almost merge into a unique flattened maximum is that the repulsion with the corresponding charge concentration maxima of the

neighboring P atoms along the  $c$  axis is decreased this way. In  $\text{FeP}_2$  the cell is significantly and visibly shrunk along the  $c$  axis; if the VSCC maxima on each P pointing towards the  $\text{Fe}_{\text{eq}}$  atoms were not flattening and not rotating towards each other, they would experience a largely enhanced repulsion with respect to the case of  $\text{FeS}_2$  (compare in Figure 2.14, middle left and right contour plots).

## 5. Conclusions

This paper disentangles the peculiar and subtle interplay between geometry, electronic structure and bonding interactions in two marcasites and löllingites prototypical compounds. This goal was in part achieved by performing DFT periodic calculations on  $\text{FeS}_2$  and  $\text{FeP}_2$  followed by a comparison of the predictions of ligand field theory against the description given by an orbital-based analysis and by the composition of bonding and antibonding states close to the Fermi level. The most illuminating and comprehensive picture was yet obtained through the analysis of the topology of two observables, the electron density and the electron density Laplacian, using the QTAIM approach. In particular, qualitative and quantitative information on the valence electron distribution anisotropy of the iron is obtained in terms of the topology of the Laplacian density, and especially so when compared to the portrait of the corresponding topology for an idealized octahedral  $t_{2g}^6$  model of the iron metal atom.

So far, in the literature, the differences between the bonding interactions in the  $M$  and  $L$  type of compounds were essentially ascribed to the extent of charge transfer from the transition metal to its linked anions and to the resulting modifications of the metal  $d$ -electrons asphericity. The charge transfer is instead found to be quite small and comparable in both compounds, in contrast to the expectations of the LFT, but in accord with electronegativity scales. Indeed, what mainly distinguishes the two compounds is the kind of anisotropy of the electron density around the iron

atom and, therefore, in how the metal  $d$  orbitals are distinctively populated. The cubic arrangement of charge concentrations around the iron atom in  $\text{FeS}_2$  transforms to a cuboid shape in  $\text{FeP}_2$ , with charge concentrations being directed towards the X anions rather than in between them in the equatorial plane. In  $M$  compounds, electrons are distributed preferentially according to the dictate of LFT for a (distorted) octahedral environment (though a significant electron population is also found in the  $e_g$  orbitals,  $x^2-y^2$  and  $z^2$ ) whereas in the  $L$  systems the  $x^2-y^2$  and  $xy$  orbitals interchange their roles. Such different charge concentrations or orbital's population distributions are, rather than the result of the geometry change from  $M$  to  $L$  compounds, essentially driven by the nature of the anion (or ligand). Pnicogens, having one less electron, are able to bond to the iron with much higher covalent character than chalcogens do. Indeed, when  $\text{FeS}_2$  is forced to adopt the  $L$  geometrical structure of  $\text{FeP}_2$ , although the changes occur in the expected direction from  $M$  to  $L$  compounds, only a very partial electron density rearrangement around the iron can be observed.

As clearly revealed by the greater uniformity of charge concentrations around X (Laplacian density topology), Fe-X and X-X bonds are significantly more alike to each other when X is a pnicogen than when it is a chalcogen. The enhanced covalent character of the Fe-X bonds when X is a pnicogen is also evident from all other kinds of analyses that were performed. On going from  $\text{FeS}_2$  to  $\text{FeP}_2$  a noteworthy change in the  $d$  orbital populations of iron, in the energy location and orbital composition of the DOS profiles, and finally in the electron density topology, was observed. These changes correspond to an increased (decreased) weight of X  $p$  orbital contributions to the bonding (antibonding) states close to the Fermi level, a diminished charge transfer and a clearly enhanced covalent character of Fe-X and X-X bonds.

To summarize, the LFT predictions are better recovered in the case of  $\text{FeS}_2$  than they are for  $\text{FeP}_2$  because in the former compound the anion is of a nature that is closer to the assumption of a

negative ligand inherent to the LFT while in the latter the anion departs more significantly from such assumption being more prone to covalent interactions.

Careful X-ray diffraction experimental studies, aimed at obtaining charge-density quality data of a number of  $M$  ( $X=S$ ) and  $L$  ( $X=P, As, Sb$ ) crystals, are currently underway in the laboratory of the Chemistry department of the Aarhus University. Obtaining a meaningful charge density for these systems is quite challenging in view of their relatively high symmetry and, more importantly, of the small ratio of the valence to core electrons. Both these factors lead to known difficulties in the multipolar model refinement of diffraction data. When available, experimental charge densities and density Laplacian distributions will be analysed within the same topological approaches used in the present study, enabling a direct and fruitful comparison with the theoretical investigation. Two main scopes may be envisaged through this coming analysis. On the one hand, to test whether the interesting description and conclusions put forth by the theoretical approach, like the change in  $d$  orbital populations and in the metal VSCC shape on passing from  $M$  to  $L$ , are sufficiently stable against the ambiguities and freedom inherent to the treatment of the experimental data. On the other hand to investigate whether crystal defects, synthesis conditions, presence of impurities, etc. could play some role in the delicate electronic balance leading to the peculiar metal asphericities and metal-ligand bonding features in the  $M$  and  $L$  compounds.

## Chapter 3

# Hypervalency in $\text{K}_2\text{SO}_4$

### 1. Introduction

A cornerstone in chemistry is the ability to predict how and why bonds are formed between atoms leading to the rich variety of compounds that constitute the world we live in. Understanding the principles behind chemical bonding is therefore crucial for any chemist. The Lewis theory is one of the most basic and widespread theories on chemical bonding and it typically appears in introductory chemistry text books.<sup>39</sup> However, cases can be found for which the octet rule, and thus this model, is violated because the central atom in a molecule has more than eight electrons in its valence shell. Such compounds are called *hypervalent*. The sulfate ion,  $\text{SO}_4^{2-}$ , is an example of an entity that is hypervalent according to the Lewis model. The hypervalency results from the introduction of double bonds in the structure leading to a count of 12 valence electrons for sulfur as indicated in Figure 3.1. The idea of double bonds and thereby hypervalency is supported by the short S-O bond lengths generally found from experiment and theory. An alternative description of the sulfate ion involves only single bonds and this avoids the issue of hypervalency (Figure 3.1). However, this description does not fulfill the Lewis requirement of minimizing the formal charges. The hypervalent picture is expected to involve the presence of several resonance forms as opposed to the single bond case. Furthermore, the number of lone pairs on the oxygen atoms differs in the two cases. This means that a characterization of the bonding and the number of lone-pairs in the sulfate group can give the information concerning which picture is more correct. However, since both in the hypervalent and in the single-bonded situation (Figure 3.1) all oxygen atoms would anyhow reflect the resonant or “static” occurrence of three lone pairs in their valence shell, only the form

and magnitude, rather than the number, of lone pair charge density concentrations should be affected.

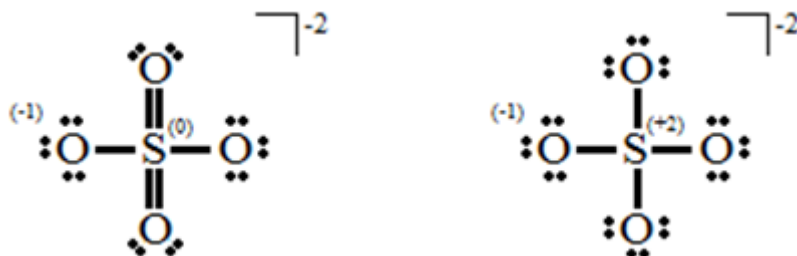


**Figure 3.1** Hypervalent (left) and single-bonded (right) depiction of the bonding situation in a sulfate ion,  $\text{SO}_4^{2-}$ . Only one of the resonance forms is drawn for the hypervalent case. Formal charges are indicated in brackets.

Several studies, both experimental and theoretical, have focused on S-O interactions and the ‘hypervalent’ character of sulfur.<sup>40,41,42</sup> One of the arguments in favor of the hypervalent description is the inclusion of the  $3d$ -orbitals on sulfur. In this picture the  $d$  orbitals should be capable of accommodating the additional valence electrons on sulfur. Theoretical calculations have proven the necessity to include the  $3d$  orbitals in the sulfur basis sets used for the calculations.<sup>43</sup> However, as pointed out by Cioslowski and Surján this could also reflect the need to include polarization functions in the optimization in order to properly describe the effects of bond-formation. The general conclusion made by Cioslowski and Surján for the ‘hypervalent’ molecules in their study is that “each of the formally double S-O bonds consists of one highly polarized covalent bond and one almost fully ionic bond.”<sup>44</sup> This is a description where the octet rule is *not* violated. A similar view on the S-O bonding is given by Dobado *et al.* that characterize it as ‘polar single  $\sigma$ -bonds mainly characterized by electrostatic interactions’.<sup>41</sup>

This chapter reports the results obtained from the study of the electron density of a sulfate containing crystalline compound,  $\text{K}_2\text{SO}_4$  (Figure 3.2) which is chosen since it is highly ionic so that the actual charge of the sulfate group is close to the formal charge of -2.

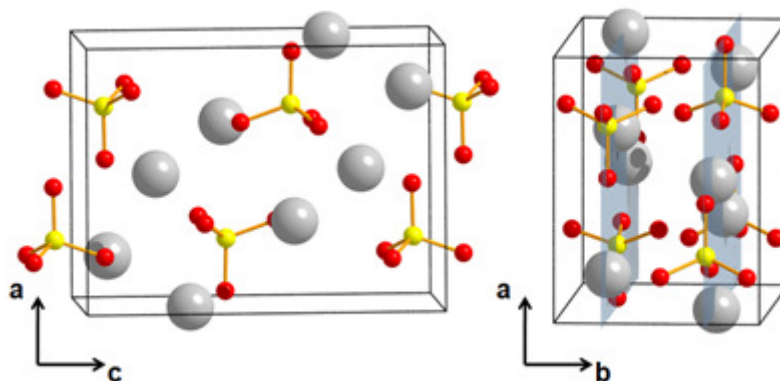


**Figure 3.2**  $\text{K}_2\text{SO}_4$  crystal structure.

The main aim of this study was to experimentally confirm the results found in the various theoretical studies and to resolve the issue of the S-O bonding that has led to the theories of hypervalency. However, even though  $\text{K}_2\text{SO}_4$  is a simple compound, it presents a substantial challenge to experimental charge density determination due to the quite severe extinction observed for the low order reflections.<sup>45</sup> Accurate measurement of these reflections is important since they carry the majority of the valence electron information. Use of a high energy, high intensity synchrotron beam makes it possible to carry out accurate diffraction experiments on micron sized crystals ( $\sim 30 \mu\text{m}$ ) with much reduced absorption and extinction effects compared with conventional sources.<sup>46</sup>

Mette S. Schmøkel (PhD stud., Århus university - DK) performed all the experimental work, including data collection, reduction and modeling of the experimentally derived charge density. To this purpose, the multipole refinement approach as implemented in the *XD2006*<sup>47</sup> program package was adopted, and the programs *TOPXD* and *XDPROP* were used to perform the topological analysis. Unless needed for the discussion, no experimental details will be reported

## 2. Computational details

The theoretical electron density has been obtained from periodic *ab-initio* DFT calculations performed employing the program CRYSTAL06.<sup>16</sup> Basis sets of def2-TZVP quality<sup>17</sup> were used for the various atoms along with the B3LYP functional. In order to avoid issues related to quasi-linear dependence of the basis set, the most diffuse *s*, *p* and *d* Gaussian functions for the K atom were removed.<sup>16</sup> No modifications have been performed for the O and S basis set. The overall (*s/p/d*) contraction scheme therefore was: K (8421/631/11), S (73211/51111/21), O (62111/4111/11). The wavefunction was evaluated at the experimental geometry determined by Mette S. Schmøkel.

Additionally, two different optimization strategies were considered. Firstly, the atomic positions were optimized keeping cell edges fixed at the experimental values. Then, both atomic positions and lattice parameters were optimized while retaining the *Pnma* space group symmetry. No significant differences have been found when evaluating electronic and topological properties from the three different periodic wavefunctions. In the following, only the results obtained from the wavefunction evaluated at the experimental geometry will be discussed.

The topology of the density was analyzed using the beta version of the program TOPOND08.<sup>48</sup>

## 3. Results and Discussion

The main topological parameters are listed in Table 3.1 and a structural drawing depicting the critical points is shown in Figure 3.3. A few discrepancies can be found between experiment and theory. The first general considerations concern the number of critical points. For the theoretical density the Morse relation  $n-b+r-c = 0$  (*n*, *b*, *r* and *c* being the number of attractors, bond (BCP), ring and cage critical points respectively) is fulfilled.<sup>49</sup>

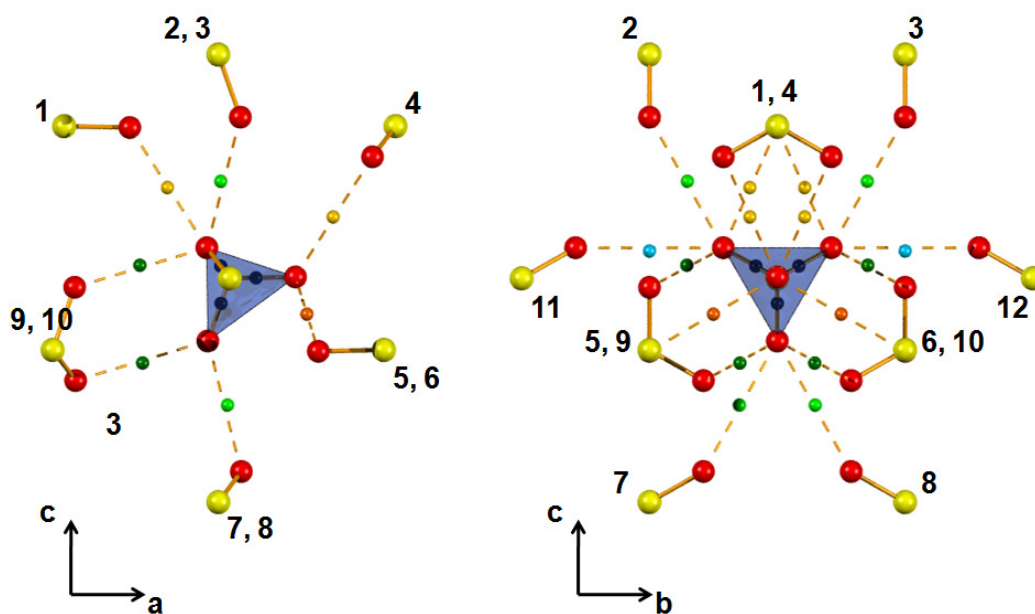


**Figure 3.3** S-O and O-O bonding interactions within and between the sulfate groups obtained from the theoretical electronic density. Big yellow and red spheres represent S and O atoms respectively. The small colored spheres represent the bcp position: B15 = bright green, B16 = green, B17 = orange, B18 = yellow, B19 = sky blue, S-O bcp = black. The numbers helps in identifying the (secondary) sulfate groups surrounding the central one. Some oxygen atoms have been removed from the secondary groups for the sake of clarity.

When considering the experimental electron density, a few critical points found in the theoretical density are missing. Alternative critical points, replacing the missing ones, could not be located, although they unavoidably exist, in order to fulfill Morse's relation (valid also for experimental densities derived through a multipolar moment model approach since an analytic function and its derivatives are eventually calculated). The missing BCPs are related to the longest (more than 3 Å) K2-O2 and O1-O3 interactions. As can be seen in Figure 3.4 the electron density and its Laplacian are almost entirely flat in the region of these BCPs. Given the number and complexity of the chemical interactions in  $\text{K}_2\text{SO}_4$  it is likely that the apparent lack of the mentioned critical points in the experimental density is due to numerical inaccuracies.

**Table 3.1** Topological parameters for the different chemical bonds based on the experimental (first line) and theoretical (second line) charge density. AIL ( $\text{\AA}$ ) is the length of the atomic interaction line.  $\rho$  is the electron density ( $e/\text{\AA}^3$ ),  $\nabla^2\rho$  the Laplacian ( $e/\text{\AA}^5$ ) and  $\varepsilon$  the ellipticity of the bond. The labels B1 to B19 are used throughout the text to identify the various BCPs.

		AIL <sub>S-bcp</sub> ( $\text{\AA}$ )	AIL <sub>bcp-O</sub> ( $\text{\AA}$ )	$\rho$ ( $e/\text{\AA}^3$ )	$\nabla^2\rho$ ( $e/\text{\AA}^5$ )	$\varepsilon$
S-O1	exp	0.591	0.889	2.017	-0.213	0.014
(B14)	opt	0.590	0.891	1.943	10.221	0.004
S-O2	exp	0.588	0.879	2.038	1.280	0.018
(B12)	opt	0.585	0.882	1.988	12.355	0.004
S-O3	exp	0.591	0.885	2.031	1.107	0.076
(B13)	opt	0.588	0.889	1.957	10.817	0.004
O1-O3	exp	-	-	-	-	-
(B15)	opt	1.721	1.714	0.027	0.351	3.363
O1-O3	exp	-	-	-	-	-
(B16)	opt	1.751	1.750	0.025	0.306	1.879
O2-O2	exp	1.671	1.671	0.037	0.363	0.229
(B17)	opt	1.670	1.670	0.034	0.422	0.071
O2-O3	exp	1.695	1.730	0.035	0.304	0.447
(B18)	opt	1.696	1.710	0.028	0.353	0.138
O3-O3	exp	1.651	1.651	0.037	0.368	0.419
(B19)	opt	1.656	1.656	0.031	0.426	0.313
K1-O2	exp	1.394	1.297	0.116	1.914	0.004
(B1)	opt	1.388	1.302	0.105	2.047	0.000
K1-O1	exp	1.469	1.412	0.086	1.275	0.189
(B2)	opt	1.445	1.433	0.082	1.440	0.067
K1-O3	exp	1.476	1.426	0.084	1.227	0.221
(B3)	opt	1.453	1.444	0.078	1.380	0.085
K1-O3	exp	1.529	1.530	0.069	0.918	0.851
(B4)	opt	1.513	1.529	0.060	1.015	0.332
K1-O3	exp	1.531	1.549	0.070	0.925	1.319
(B5)	opt	1.516	1.539	0.060	1.026	0.669
K2-O1	exp	1.392	1.312	0.117	1.961	0.073
(B6)	opt	1.371	1.332	0.119	2.159	0.024
K2-O3	exp	1.402	1.305	0.111	1.865	0.005
(B7)	opt	1.395	1.313	0.103	1.978	0.014
K2-O3	exp	1.422	1.345	0.102	1.668	0.048
(B8)	opt	1.402	1.365	0.103	1.828	0.050
K2-O1	exp	1.424	1.331	0.101	1.660	0.008
(B9)	opt	1.419	1.336	0.092	1.759	0.013
K2-O2	exp	1.466	1.409	0.085	1.338	0.297
(B10)	opt	1.446	1.426	0.082	1.473	0.137
K2-O2	exp	-	-	-	-	-
(B11)	opt	1.549	1.557	0.050	0.873	1.051

This is also supported by the fact that the profiles of the Laplacian along the different interatomic distances is very similar for experiment and theory. For all the K-O and O-O interactions the Laplacian profiles are similar to the one shown in Figure 3.4. The BCP is located far from the atomic valence shell charge concentrations (VSCCs) and the value of  $\rho$  is very low. This, combined with positive values of the Laplacian at the BCP, is an indication that these interactions have the expected closed shell nature.

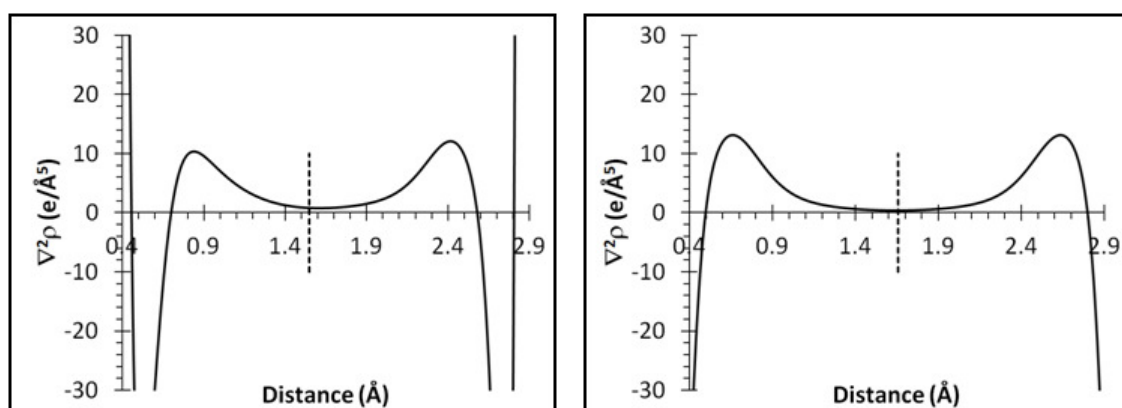


**Figure 3.4** Laplacian profiles along the K-O (left) and O-O (right) interaction lines in the crystal. The dotted vertical line marks the position of the bond critical point (bcp). On the x axes is reported the distance from the origin (in the left picture the K atom is placed at the origin).

In contrast to this, the profiles for the S-O interactions are different and also show some deviation between experiment and theory (Figure 3.5). The experimental Laplacian values at the BCPs for the three S-O interactions (Table 3.1) would indicate a different description for the three bonds. In fact, just considering the sign of these values would indicate a shared shell interaction for S-O1 and closed shell interactions for S-O2 and S-O3. However, the values are rather small and therefore do not adequately assess the nature of the bonds. In contrast, the three theoretical values are similar in magnitude and clearly positive. The reason for the discrepancies in the Laplacian values at the S-O BCP is made clear in Figure 3.5. The Laplacian is quite steep around the position of the BCP and, as a consequence, a small variation of the position of the BCP will change the Laplacian drastically

and may even change the sign of it. The overall picture of the S-O bonding obtained from the Laplacian profiles is that charge accumulation can be observed in the region between the two types of atoms. Yet, due to the large charge transfer between S and O atoms, this region fully belongs to the oxygen atom basin. In Figure 3.6 a comparison is made between the Laplacian profiles for free and bonded atoms. It is seen that the general shape of the sulfur and oxygen VSSC can still be recognized in the molecule. However, the sulfur atomic VSSC is upon bond formation fully attributed to the oxygen atomic basins. As a consequence, and in accordance with the different electronegativities of the S and O atoms, the major part of the electronic charge participating in the S-O bonding is shifted towards the oxygen. The positive value found in some cases for the Laplacian at the BCP is simply due to the fact that the BCP is located in the region of charge depletion of the sulfur atom.

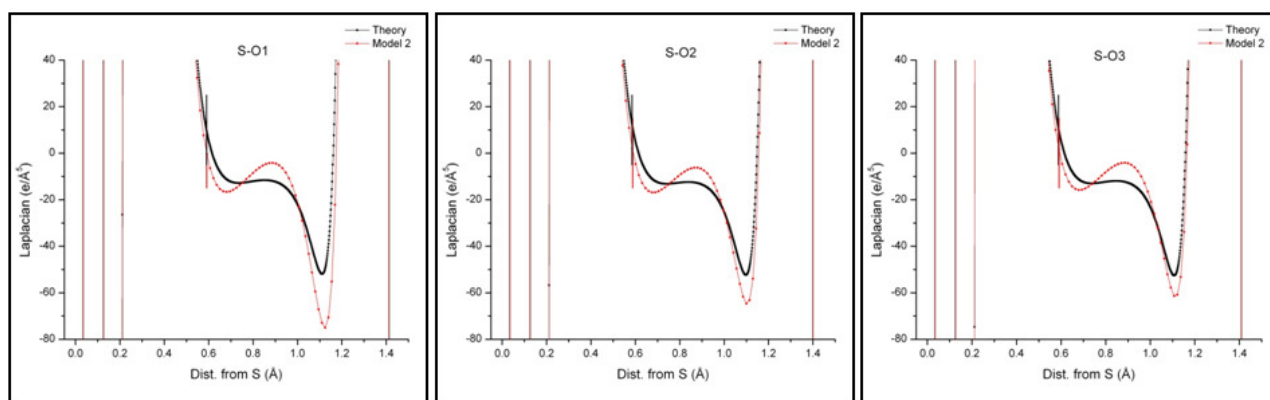


**Figure 3.5** Laplacian profiles along the three S-O interaction lines in the crystal for the theoretical and the experimental data. The dotted vertical line marks the position of the bond critical point (bcp). On the x axes is reported the distance from the origin and in each picture the S atom is placed at the origin.

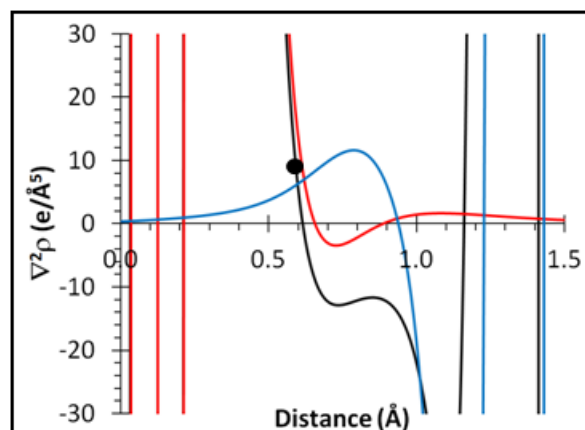


**Figure 3.6** Laplacian profiles along the S-O1 interaction lines in the crystal for the theoretical data. The profiles portrayed refers to the crystal (solid black) and to the isolated atoms (S: solid red; O: solid blue) Laplacian densities. The black dots mark the position of the bond critical point (bcp) in the crystal. On the x axes is reported the distance from the origin.

Even though the details differ the overall picture of the S-O bonding is consistent for the experimental and theoretical densities. For all S-O bonds localized charge accumulation is observed in the region between the two atoms which is characteristic of a shared-shell interaction. Furthermore, the BCPs are located closer to the less-electronegative sulfur atom indicating a highly polarized bond. Also, they are found to lie close to the Laplacian zero-contour region as seen in Figure 3.5. This is a clear proof of the transfer of charge from sulfur to oxygen. The profile of the Laplacian along the S-O bonds shows two local minima and a local maximum (i.e. a ‘double dip’ in  $\nabla^2\rho$ ) in the region of the BCP. In a previous study such a feature has been taken as an indication of covalent character of the bonding.<sup>42</sup>

This description of the S-O bond is supported by the two-dimensional contour plots and three-dimensional isovalue surfaces of the Laplacian of the electron density of the sulfate group in Figures 3.7 and 3.8. Four VSCC maxima and associated regions (that is their irreducible domains) are found around sulfur directed towards the surrounding oxygen atoms and essentially belonging to these atoms, since the  $-\nabla^2\rho$  maxima are located in their basins. From the contour plots in Figure 3.7,

three charge accumulations can be envisaged within the VSCC of each oxygen atom. It is tempting to identify these with two oxygen lone-pairs and the S-O bonded concentration. From the three-dimensional isovalue Laplacian surfaces in Figure 3.8 it is not easy to identify localized regions of charge accumulation for the oxygen atoms. Only for O3, and using a contour level as high as  $-85e/\text{\AA}^3$  it is possible to see three distinct accumulation regions.

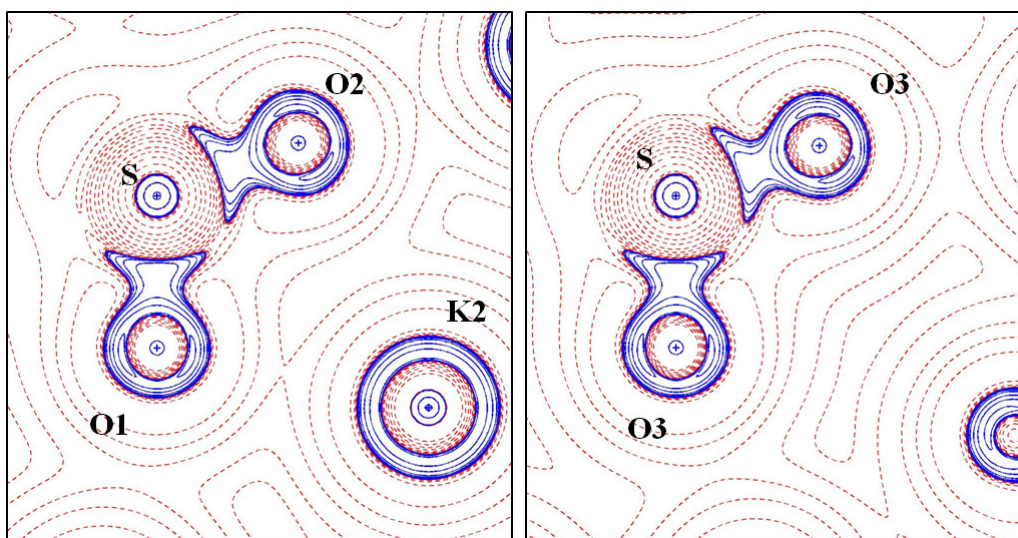


**Figure 3.7**  $\nabla^2\rho$  maps cut in the O1-S-O2 (left) and (O3-S-O3) right plane of the crystal. Solid blue line mark regions of charge accumulation (negative  $\nabla^2\rho$ ) while dotted red lines mark regions of charge depletion (positive  $\nabla^2\rho$ ).

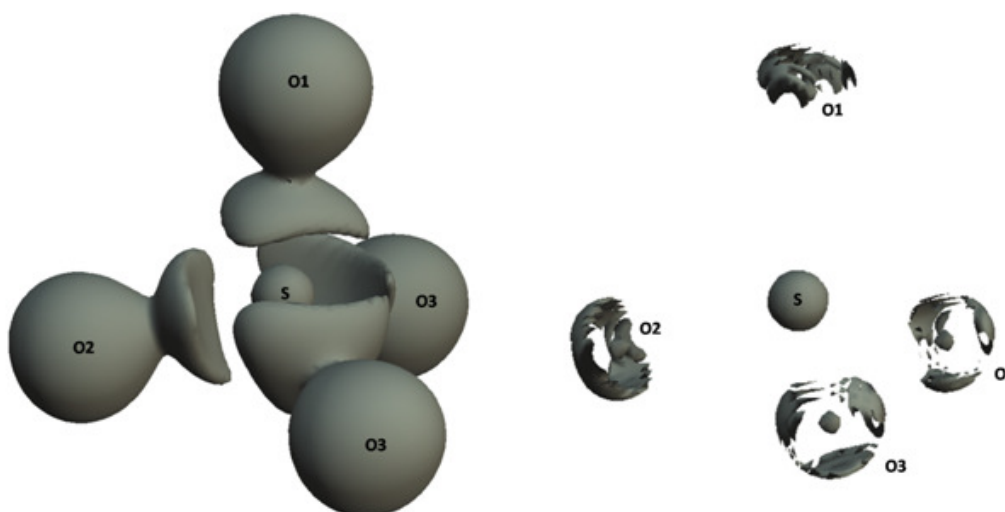


**Figure 3.8** Three-dimensional plots of the Laplacian at contour levels of zero (left) and  $-85 e/\text{\AA}^3$  (right) for the experimental density.

In order to more adequately identify VSCC maxima and their associated regions around the oxygen atoms, a topological search for the (3,-3) critical points in the negative Laplacian has been performed and the resulting VSCC are listed plotted in Figure 3.9 for the theoretical density. Only the theoretical results are shown here whereas the experimental ones can be found in the Supporting Information. The results reveal the presence of three maxima pointing away from the S-O bond for all oxygen atoms. These are usually indicated as *non-bonding maxima* (NBM) and are associated with lone pairs in the Lewis theory. An additional (3,-3) CP is found for O2 along the S-O interaction line, while one (3,-3) maximum is found along each S-O bond, located in the O basin, close to the S-O bcp and the S | O interatomic surface. These maxima, lying along the bond paths, are referred to as *bonding maxima* (BM). The presence of these BM and NBM accounts for the  $sp^3$  hybridization of the oxygen atoms, thus in agreement with the picture of a single and, because of their location, polarized S-O bond. However, as said before, three NBM would also be compatible with the situation in which some mixing of the two forms in Figure 3.1 occurs and possibly even for the ensemble of the resonant forms corresponding to the pure hypervalent description. For the S-O1 and S-O3 interactions, only one BM is found between these atoms, probably due to enhanced electron sharing. This is at first surprising since one would expect such a situation for the shortest interaction, which is S-O2, but it may be easily rationalized in consideration of the fact that a bond length decrease leads to a more polarized S-O bond (*see infra*).

An almost identical picture is obtained from the experimental data. The only major difference is that for O2 only two VSCC regions pointing away from sulfur are found. This is to be expected since, as seen from Figure 3.7, they are both positioned in the mirror plane. If an additional maximum was to be found outside of the plane this would have to appear twice (due to the mirror plane symmetry) giving a total of 5 VSCCs for O2 (including the BM). This discrepancy between theory and experiment needs a further analysis, not yet concluded at the time of writing this thesis. It requires



obtained from theoretical calculations the Bader net atomic charges obtained are very similar. The net charge on S is around +4 which is slightly higher ( $\sim 0.4$ ) than the experimental value. Similarly the potassium net charges obtained from theory are slightly higher at  $\sim 0.9$  compared with  $\sim 0.75$  from experiment. Cioslowski and Surján interpret their large Bader atomic charges in S-O containing compounds as proof of a large degree of ionicity in the bonds.<sup>44</sup> Our results point in the same direction with the knowledge that the huge charge separation is actually due to strong polarization rather than an ionic description of the bond.

**Table 3.2** Bader's electron populations,  $N(\Omega)$ , and net charges,  $q(\Omega)$  for the experimental and theoretical charge densities .

Atom $\Omega$		exp	theo
K1	$N(\Omega)$	18.28	18.1
	$q(\Omega)$	0.72	0.90
K2	$N(\Omega)$	18.23	18.1
	$q(\Omega)$	0.77	0.90
S	$N(\Omega)$	11.73	12.14
	$q(\Omega)$	4.27	3.86
O1	$N(\Omega)$	9.37	9.42
	$q(\Omega)$	-1.37	-1.42
O2	$N(\Omega)$	9.39	9.41
	$q(\Omega)$	-1.39	-1.41
O3	$N(\Omega)$	9.43	9.42
	$q(\Omega)$	-1.43	-1.42

As a final characterization of the bonding features in  $K_2SO_4$  using only electron density based descriptors, the Source Function (SF) contributions from the various atomic basins have been evaluated for the theoretical electron density.<sup>50</sup> In Table 3.3 the percentage contribution, %SF, to the electron density at the various S-O BCPs is reported.

**Table 3.3** %SF contributions to S-O BCPs. The symbol O3 $_{\sigma}$  identify the oxygen atom equivalent to O3 due to the presence of the mirror plane.

BCP	Bond	S	O1	O2	O3	O3 $_{\sigma}$	TOT
B14	S-O1	28.5	49.4	6.8	6.7	6.7	98.2
B12	S-O2	29.5	6.4	50.0	6.5	6.5	98.9
B13	S-O3	28.6	6.6	6.8	49.6	6.6	98.3
	S- O3 $_{\sigma}$	28.6	6.6	6.8	6.6	49.6	98.3

As can be seen about 79% of the density at the BCP is determined by the sulfur and its linked oxygen atom. This value is comparable to that found for a prototypical covalent bond such as the C-C single bond in ethane<sup>50b</sup> and indicates that the valence charge involved in bonding is localized, though not as much as found in conventional covalent double bonds (%SF around 85-90%). The large difference between the %SF values for S and O, with the linked O determining almost twice the density contributed by the S atom at the bcp, clearly denotes the largely polarized nature of the S-O shared bond. Not to be neglected is the density contribution determined by the oxygen atoms within the same sulfate group not directly involved in the bond (Table 3.4). Such cumulative contribution amounts to about 20% of the S-O bcp density, that is about 2/3 of the density determined at the same point by the sulphur atom. This is perhaps an unexpected result in view of a single-bonded depiction of the bonding in the sulfate ion (Figure 3.1, right) and one could naively tempted to ascribe it just to the proximity of the oxygen atoms and to the inverse dependence from the distance to the reference point in the local source function expression.<sup>50</sup> However, the importance of the neighboring oxygen atoms is neatly corroborated by the appreciably large electron exchange existing between oxygen atoms, as expressed by the values of the delocalization indices<sup>50b</sup>  $\delta(O,O')$ . Evaluation of such indexes requires the pair density, not available at the experimental level, and expressed only in terms of the first order density matrix within a single determinant approach (at Kohn-Sham DFT level the approximate formula that makes use of an HF-like second-order exchange density matrix is customarily adopted). Table 3.4 reports %SF and

$\delta(\text{O},\text{O}')$  values calculated for a  $T_d$  molecular model of the sulphate group, at the equilibrium S-O distance (B3LYP/6-311G++(d,p) level) and for an elongated and a shortened S-O bond distance. Reported in this table are also the net charge on the oxygen atom and the value of the Laplacian at one of the three equivalent oxygen lone pairs concentrations nbm, as they both change with distance. Before discussing data in Table 3.5, we just recall that the number of electrons on an atom  $\Omega$ ,  $N(\Omega)$ , may be seen as given by the sum of those who are localized within the basin,  $\lambda(\Omega)$ ,

$$N(\Omega) = \lambda(\Omega) + \frac{1}{2} \sum_{\Omega' \neq \Omega} \delta(\Omega', \Omega) \quad \text{Eq. 1}$$

and those that are delocalized (exchanged) between them (second term in the right-hand expression of Eq. 1). For typical single, double and triple covalent bonds, like the CC bond in ethane, ethene, ethine  $\delta(\text{C},\text{C}')$  are almost equal to one, two and three. When a bond is largely polarized, electrons are less effectively exchanged and, for instance, a  $\delta(\text{C},\text{O})$  value of about 1.6-1.8 is observed for the  $\text{C}\equiv\text{O}$  molecule. Let's so first consider the S-O bond at the equilibrium distance:  $\delta(\text{S},\text{O})$  is 0.96 and S and O are exchanging about one electron as expected for a covalent single bond or for a highly polarized single bond with partial double bond character. The number of electrons delocalized between each pair of oxygen  $\delta(\text{O},\text{O}') = 0.23$  is not negligible and the sum of electrons each oxygen exchanges with the neighboring oxygen atoms in the sulphate group is only 20-30% less than the electron charge it exchanges with the sulphur atom to which is directly bonded! When the S-O bond is forced to shorten or elongate, the contribution of the various resonant forms of the hypervalent bonding scheme (Fig. 3.1, left) is expected to respectively increase and decrease and a similar trend should thereby be observed as for the capability of the oxygen atoms to exchange electrons between themselves.<sup>c</sup>

---

<sup>c</sup> Note that the evaluation of the ellipticity at the bcp, or at any point along the bond path, does not provide information about double-bond character in such case, since  $T_d$  symmetry implies a perfect cylindrical symmetry around the bond, regardless of its actual bond order. A similar

**Table 3.4** %SF contributions for the S-O BCP in a  $T_d$  model for the sulphate group at equilibrium (1.53Å), shortened and elongated bond distance. Delocalization indices  $\delta$ , the net oxygen charge  $q(O)$  and the value of the negative of the Laplacian density at one of the three equivalent oxygen lone pairs concentrations, NBM, is also reported for the various S-O distances.

d (Å)	$\rho$ ( $e/\text{Å}^5$ )	%SF (S)	%SF (O)	$\Sigma_{O'}\%$ SF (O')	$\delta(S,O)$	$\Sigma_{O'} \delta(O,O')$	$q(O)$	NBM ( $e/\text{Å}^5$ )
1.47	1.92	27.1	49.8	21.6	0.87	0.74	-1.46	92.8
1.53	1.78	31.8	48.0	20.1	0.96	0.68	-1.37	96.2
1.59	1.63	36.9	45.3	17.4	1.08	0.61	-1.23	100.3

Indeed (Table 3.4) the bcp density is largest for the shortest distance and smallest for the elongated geometry, suggesting an enhanced “double-bond” character with S-O distance shortening. Furthermore, the trend of the  $\delta(O,O')$  values indicates that the capability of the oxygen atoms to exchange electrons between oxygen atoms increases with decreasing S-O distance and an analogous trend is observed for the %SF contribution from neighboring oxygen atoms to the S-O bcp density. The increased availability of electrons in the bonding region with decreasing S-O distance is also revealed by the parallel decrease of the electronic charge concentration of the lone pairs as indicated by the significant decrease of the magnitude of the  $-\Delta\nabla^2\rho$  NBMs. However, one also note that unexpectedly the electron exchange between S and O (and thus the bond order) largely diminishes with decreasing S-O distance, rather than increasing as also corroborated by the decreasing percentage contribution from the S and O atoms to the density at their intervening bcp. The  $\delta(S,O)$  value diminishes from 1.08 at R equal to 1.59 Å to 0.87 at R equal to 1.47 Å, while the sum of %SF contributions from the oxygen and the sulphur atoms show a parallel decrease from 82.2 to 76.9%. What is very interesting is to observe that the decrease of  $\delta(S,O)$  and of the %SF(S+O) contribution

---

situation holds also for any situation which is a slight perturbation with respect to the  $T_d$  symmetry, as it is the case of our experimental geometry .

is accompanied by a clear increase of the bond polarity, since the ratio of sources from sulphur and oxygen atoms lowers from 0.81 at  $R$  equal to 1.59 Å to only 0.54 at  $d$  equal to 1.47 Å. Note that an homopolar bond would have a ratio of 1 at any distance. In other words, the SF not only mirrors the changes in the electron density exchange described by the delocalization indices, but also provides a rationale for such changes. The unexpected electron delocalization decrease with decreasing distance is the result of a strongly enhanced bond polarization, as also indicated by the largely increased charge transfer with decreasing distance ( $Q(O)$  values in Table 3.4).

Overall, when forcing an increase of the contribution of the various resonant forms of the hypervalent bonding scheme, the S-O bond order is found to decrease rather than increase because of the counterbalancing effect due to the largely enhanced bond polarity. The electronic charge withdrawn from the lone pair regions and made available in the S-O bonding region turns out yet to be essentially localized on the oxygen basins, a fact which explains why oxygen atoms increase their ability to exchange electron among themselves, despite their decreased electron exchange with the sulphur atom. This mechanism while clearly ruling out any hypervalent description of the sulfur atom in the sulfate group, does not deny the possibility of an appreciable electron exchange among the oxygen atoms of this group, due to a partial contribution of resonant forms having a so polarized “double-bond” character that the actual S-O bond order at equilibrium does not exceed that of a standard covalent single bond.

#### 4. Conclusions

The S-O bonding has been investigated through a study of the charge density of the sulfate group,  $SO_4^{2-}$ , within a crystalline environment, using both experimental and theoretical electron densities. The experimental charge density was determined by multipole least squares refinement, while a theoretical density was obtained from periodic *ab-initio* DFT calculations. The chemical bonding

was analysed within the framework of the Quantum Theory of Atoms In Molecules (QTAIM). The Source Function topological descriptor has also been applied to provide further insight on the electron distribution within the  $K_2SO_4$  crystal lattice. The combined evidence suggests a bonding situation where the S-O interactions can be characterized as highly polarized, covalent bonds, with “single bond” description significantly prevailing over the “double bond” picture. Model calculations on systems with shortened S-O bonds with respect to equilibrium, indicate that even when the lone pair electrons on oxygen atoms are forced to participate to bonding (formally enhancing the “double bond” character), an unexpected decrease in the S-O electron sharing is observed since a parallel increase in the charge transfer between the sulphur and the oxygen atoms occurs, leading to a further polarization of the S-O interactions. Conversely, the non negligible electron sharing among oxygen atoms already present at equilibrium, is further enhanced upon S-O bond shortening. Overall, this picture rules out the possibility of a hypervalent description of the sulfur atom in the sulfate group, despite the appreciable electron exchange occurring among the oxygen atoms of this group.

## Chapter 4

# Coordination Polymers: the case of $[\text{Zn}(\text{HCOO})_2(\text{H}_2\text{O})_2]_\infty$

### 1. Introduction

Coordination polymers (CPs) have received an enormous attention due to their broad range of properties ranging from gas-storage, porous properties, catalytic properties, negative thermal expansion and magnetic properties.<sup>51</sup> Unlike many other porous materials the reactants are preserved during the synthesis and thus, it is in principle possible to tailor the product by carefully choosing the reactants. However, it has been shown that minor changes in synthesis parameters can lead to different products,<sup>52</sup> and often the synthesis can lead to multiple products.<sup>53</sup>

A lot of experimental work has been already carried out at Århus university on this class of compounds. The studies have been mainly concerned with the magnetic properties of coordination polymers through analysis of the X-ray charge densities.<sup>54</sup> These analyses are often complicated by poor crystal quality and quite complicated structures which often include disordered solvent molecules.<sup>55</sup>

The isostructural series have been known since the 1960s<sup>56</sup> and have been studied mainly due to their interesting magnetism, which, despite a wealth of studies, is not completely understood and inconsistencies still exists. The most studied compound in the series is the Mn containing analog which shows at least three phase transitions at 3.7, 1.7 and 0.6 K.<sup>57</sup> The various experiments revealed that the Mn(1) layers order in a canted antiferromagnetic sublattice at 3.7 K. At 1.7 K this sublattice spontaneously reorients. The Mn(2) sublattice follows a Brillouin like function with only slowly increasing magnetization below the Néel temperature,<sup>58</sup> and it has therefore often been referred to as being paramagnetic down to 0.6 K. It has been suggested that the formate linkers act as superexchange pathways for the magnetic interaction.

The work reported here couples with the experimental analysis performed by Mads R. V. Jørgensen (PhD stud.) and is focused on one of the simplest coordination polymers known,  $\text{Zn}(\text{HCOO})_2(\text{H}_2\text{O})_2$ . Due to the presence of Zn, the compound is nonmagnetic and can thus be considered a reference structure aiding the understanding of the magnetic compounds in the series.

## 2. Crystallographic structure

The structure of the polymer is shown in Figure 4.1. The compound crystallizes in the monoclinic space group  $P21/c$  and is composed of Zn, formic acid residues, and water molecules. There are two distinct metal sites in the structure both located on sites with inversion symmetry. Both are coordinated in a slightly distorted octahedral field. Zn(1) is coordinated to six formate ligands, four of these create layers in the  $bc$ -plane, and all Zn atoms in these layers are interconnected with formate linkers. Zn(2) is coordinated to two formate ligands and four water molecules. This creates layers of mutually unconnected Zn(2) ions interpenetrating the layers formed by Zn(1) (Figure 4.2). The two kinds of layers are connected by formate linkers from Zn(1) to Zn(2) creating a 3D network. The hydrogen atoms on the two water molecules are all involved in hydrogen bonding (Figure 4.3). Three of these provide interaction between the Zn(1) and Zn(2) layer, while the last, shown in red in the figure, provides a contact within the Zn(2) layer.

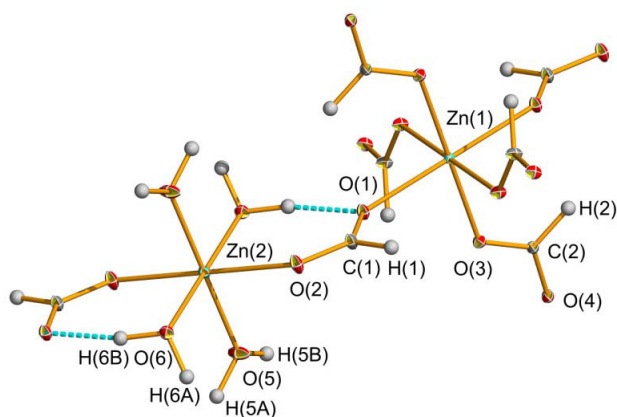


**Figure 4.1** Structure of  $\text{Zn}(\text{HCOO})_2(\text{H}_2\text{O})_2$  at 100K. The labels are only shown for atoms in the asymmetric unit. Thermal ellipsoids at 50% probability level.

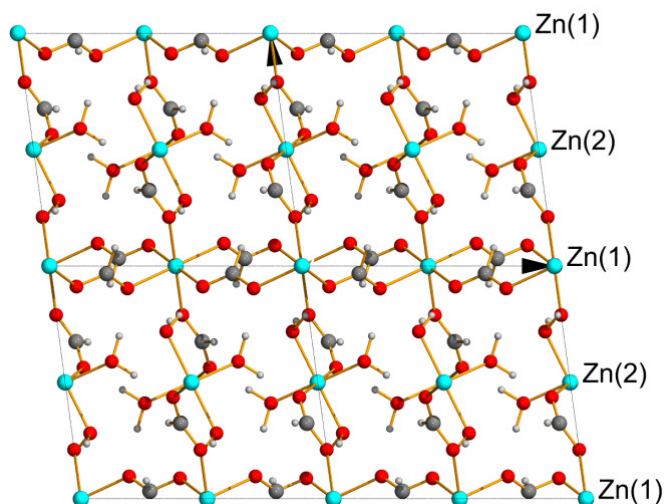


**Figure 4.2** Projection along the b-axis of the 2x2 super cell.

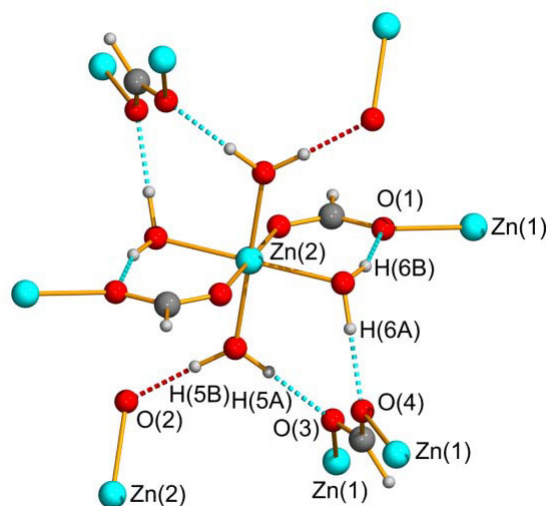


**Figure 4.3** Section of the polymer structure. The H-bonds within the Zn(2) layer are shown in red.

### 3. Computational details

The wave function was calculated using *ab initio* periodic density functional theory employing B3LYP exchange and correlation functional (Becke, 1993; Lee *et al.*, 1988) implemented in the program CRYSTAL06.<sup>16</sup> The basis set used in the calculations was a standard Pople 6-311G basis set for all atoms except Zn. The basis set for Zn was a def2-TZVP basis set,<sup>18</sup> overall corresponding to an all electron triple- $\zeta$  basis. To avoid issues related to quasi-linear dependence the coefficients

of the outermost *s* and *p* functions has been recalculated. The *f* functions have furthermore been removed. Two different geometries have been determined experimentally, based on data collected at 15K and at 100K. Both the geometries have been considered for the theoretical modelling. The energy was minimized and a criterion of  $\Delta E < 10^{-6}$  Hartree was used to ensure that the model has reached convergence. The topology of the density was analyzed using the beta version of the program TOPOND08.<sup>48</sup>

#### 4. Results and Discussion

As for  $K_2SO_4$ , no results based on the experimental work performed by Mads R. V. Jørgensen (PhD stud.) will be reported here, unless fundamental for the ongoing discussion. In any case mainly a qualitative view will be given.

To accurately model the Zn atoms from the collected data, several models were tested and the residual density was scrutinized for systematic features. In previous charge density studies of Zn containing compounds the analysis were complicated by anharmonic motion, which can correlate with the multipole parameters, thus leading to difficulties separating vibration and bonding features. This could lead to a masking of the detailed bonding features around the presumably highly spherical Zn atom. However, in this study there were no indications of anharmonic motion of the Zn atom.

From overall charge considerations the charge of each Zn atom in  $Zn(HCOO)_2(H_2O)_2$  is expected to be in a formal +2 valence state. Therefore, a plausible model would be to keep the  $3d^{10}$  shell unperturbed and refine population and possible aspherical features of the 4s electrons. Alternatively the 4s electrons could be removed completely from Zn and distributed to the surrounding oxygen atoms. This could be combined with the use of an ionic radial function. In the isostructural compound  $Mn(HCOO)_2(H_2O)_2$  it was found that there were some electron donation from the

ligands into the 3d orbitals thus leading to some perturbation of the atomic orbitals.<sup>59</sup> By analogy the ligands could potentially perturb the valence shell, thus lead to an aspherical charge distribution, not only of the 4s electrons, but also of the 3d electrons. Therefore it would be important to test if the 3d electrons were indeed perturbed. Five different models denoted **I-V**, with neutral radial functions from the SCM data bank and including 4s electrons were tested against the 100 K data. Some results are shown in Table 4.1.

**Table 4.1** Comparison of different Zn charge density models. **I**: 3d population and multipoles refined, 4s population fixed to 2e<sup>-</sup> and spherical. **II**: 3d population fixed at 10e<sup>-</sup> and 4s population refined spherically. **III**: as **II** but 4s refined aspherically. **IV**: 3d and 4s monopole populations refined, but only 3d multipoles refined. **V**: As **IV** but in addition 4s multipoles were refined.  $P_{xy}$  is the population of the  $xy$  orbital,  $R(F^2)$  is the R-value,  $\Delta\rho$  is peak value in the residual density and  $Q_\Omega$  is the integrated charge of the atomic basin.

Model	$P_{4s}$ Zn(1)	$P_{4s}$ Zn(1)	$P_{3d}$ Zn(1)	$P_{3d}$ Zn(2)	$R(F^2)$	$\Delta\rho_{\min}$	$\Delta\rho_{\max}$	$Q_\Omega$ Zn(1)	$Q_\Omega$ Zn(2)
<b>I</b>	2	2	9.99	9.96	0.0105	-0.168	0.212	0.91	0.92
<b>II</b>	1.62	1.64	10	10	0.0110	-0.269	0.269	0.74	0.71
<b>III</b>	1.69	1.75	10	10	0.0108	-0.248	0.263	0.75	0.77
<b>IV</b>	2.18	2.16	9.98	9.96	0.0106	-0.174	0.222	1.79	1.46
<b>V</b>	2.25	2.14	10.00	9.99	0.0103	-0.167	0.213	1.77	1.47

The 4s electrons of transition metals are notoriously hard to model due to their diffuse nature, and thus often only a few low order reflections will contain information about these electrons. These low order reflections are often weakened by extinction, which have been refined to a significant value for both data sets. The differences between the models are minor, yet a careful analysis of the results seemed to indicate model **I** as the one best describing the data. This was quite surprising, since it includes a filled 4s orbital in contrast to the expected +2 valence state for Zn. Also surprising was the fact that deformation densities still revealed that the Zn atoms were not completely spherical. It was encouraging to find that also the deformation densities maps obtained

from the theoretically derived electron density showed a similar structure around the metal atom (Figure 4.4).

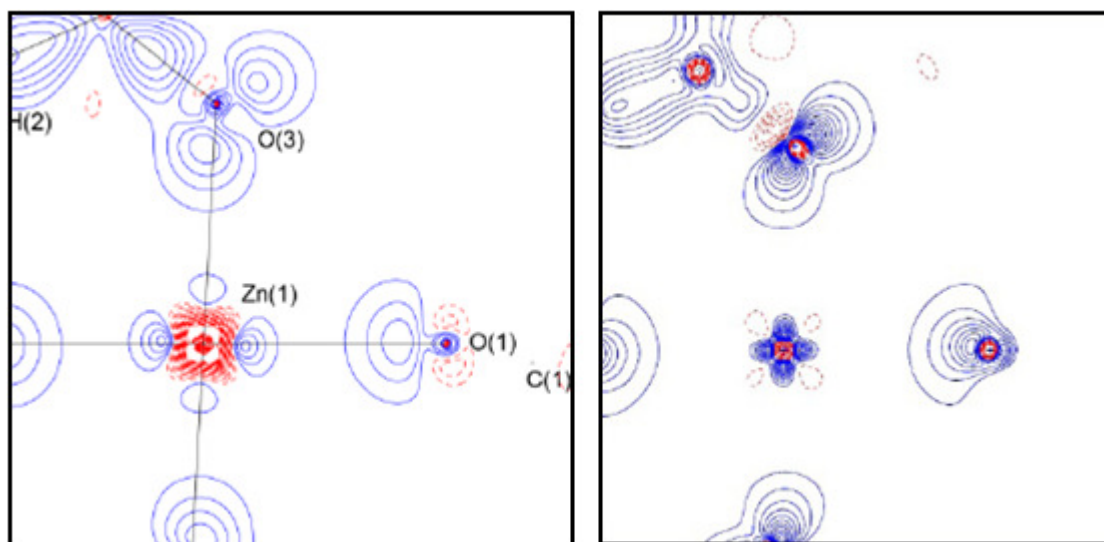


**Figure 4.4** Deformation densities maps for the experimental (left) and theoretical (right) models. Contours are plotted at  $0.1e\text{\AA}^{-3}$ , the zero contour is omitted. Blue regions represent positive values of  $\Delta\rho$ , while red regions negative values.

Of course a direct comparison of the deformation densities from the experimental models and the theoretical model is not possible as the reference models, superposition of neutral spherical atoms, are not identical and thus, only a qualitative comparison can be made. Still it is interesting to note that, besides acknowledging the asphericity of the Zn atoms, both theory and experiment highlights accumulation of density directed towards the negative ligands in the presumably rather ionic Zn-O bonds, even more so as the largest accumulations are found along the shorter ones.

Indeed this could be a sign of covalent character, thus supporting the idea that shared shell interaction are present in this compounds. However, from the topological analysis of the electron density this view seems to be lacking. For both the Zn atoms three different interactions with the surrounding oxygen atoms have been found (Table 4.2).

**Table 4.2** Topological interactions for the Zn-O bonding interactions.

Bond	d (Å)	AIL <sub>A-bcp</sub> (Å)	AIL <sub>bcp-B</sub> (Å)	$\rho$ (e/Å <sup>3</sup> )	$\nabla^2\rho$ (e/Å <sup>5</sup> )	$\epsilon$
Zn1-O4	2.0608	1.0017	1.0604	0.440	8.446	0.037
Zn1-O3	2.0957	1.0185	1.0789	0.402	7.611	0.032
Zn1-O1	2.1302	1.0341	1.0980	0.372	6.793	0.029
Zn2-O5	2.0546	0.9985	1.0564	0.438	8.729	0.069
Zn2-O6	2.0970	1.0154	1.0819	0.409	7.700	0.055
Zn2-O2	2.1644	1.0518	1.1153	0.336	6.124	0.017

In all the cases a decrease of the value of  $\rho$  is observed according to an increase of the bonding distance. The Laplacian of  $\rho$ ,  $\nabla^2\rho$ , is found to be positive for every of such interactions, suggesting that the nature of the M-O interaction is closed-shell. However, since the N shell is not revealed by the Laplacian for the considered metals,<sup>60</sup> this value can't be considered a definitive proof. Further insights can be obtained plotting the  $\nabla^2\rho$  profiles along the line joining the bonded atoms and comparing the value of the Laplacian, at the BCP, with the one that is obtained from the IAM (Independent Atoms Model) description.

This is shown in Figure 4.5 for the Zn2-O5 interaction (similar plots are found for all the Zn-O bonds) and it is evident that, upon bond formation, charge density is removed from the bonding region resulting in the positive value found for the Laplacian. Figure 4.5 also rules out the hypothesis of a highly polarized covalent bond, such as found for the S-O interactions (see Chapter 3)

A different picture arises for the C-O, C-H and O-H interactions, for which the expected shared-shell nature of the bond is found. This is supported by the high value of  $\rho$  and the negative value of  $\nabla^2\rho$  at the BCP (Table 4.3 and Table 4.4). Furthermore, the Laplacian profiles (Figure 4.6 and Figure 4.7) shows charge accumulation between the two atoms involved in the bond and, for C-O and O-H, the shift of the BCP towards the most electronegative atom reveals some degree of polarization.

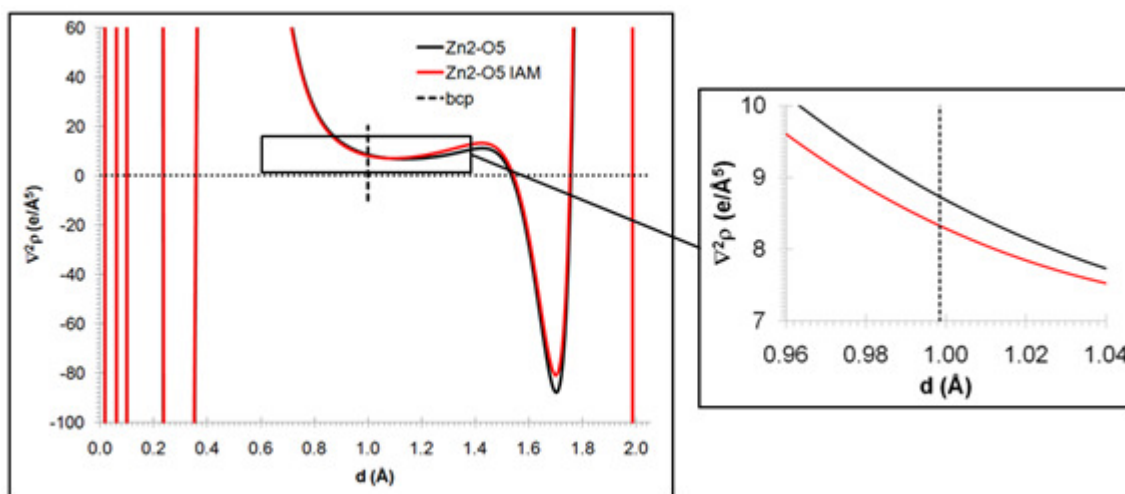


**Figure 4.5** VSCCs around Zn(1) (left) and Zn(2) (right). Magenta spheres show positions from the experimental density at 100 K and blue spheres the positions from the theoretical density. Bonds correspond to the interatomic vectors.

**Table 4.3** Topological parameters for the C-O and C-H bonding interactions in the formate ligands.

Bond	$d$ (Å)	$AIL_{A-bcp}$ (Å)	$AIL_{bcp-B}$ (Å)	$\rho$ (e/Å <sup>3</sup> )	$\nabla^2\rho$ (e/Å <sup>5</sup> )	$\epsilon$
C1-O1	1.2646	0.4554	0.8093	2.331	-13.025	0.058
C1-O2	1.2555	0.4515	0.8042	2.383	-12.869	0.044
C1-H1	1.0840	0.7186	0.3530	1.871	-20.639	0.009
C2-O3	1.2530	0.4498	0.8032	2.397	-12.717	0.046
C2-O4	1.2605	0.4537	0.8069	2.360	-13.181	0.052
C2-H2	1.0840	0.7159	0.3560	1.872	-20.511	0.008

**Table 4.4** Topological parameters for the O-H bonding interactions in the water ligands.

Bond	$d$ (Å)	$AIL_{A-bcp}$ (Å)	$AIL_{bcp-B}$ (Å)	$\rho$ (e/Å <sup>3</sup> )	$\nabla^2\rho$ (e/Å <sup>5</sup> )	$\epsilon$
O5-H3	0.9900	0.7715	0.2005	2.120	-44.058	0.019
O5-H4	0.9900	0.7671	0.2051	2.136	-43.371	0.019
O6-H5	0.9900	0.7671	0.2052	2.143	-43.554	0.019
O6-H6	0.9900	0.7667	0.2057	2.147	-43.296	0.019

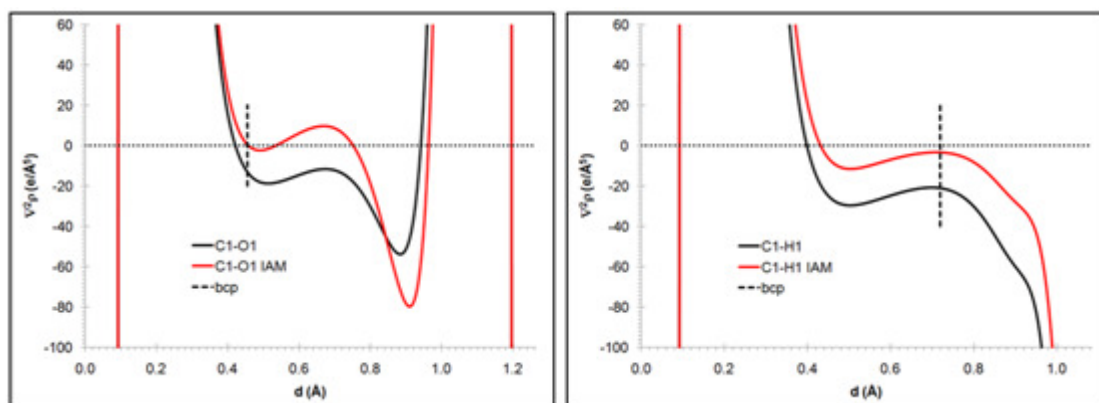


**Figure 4.6** Laplacian profile for the C1-O1 (left) and C1-H1 (right) interactions. The C atom is displayed on the left, while O/H atom is on the right. The dashed vertical line marks the position of the BCP

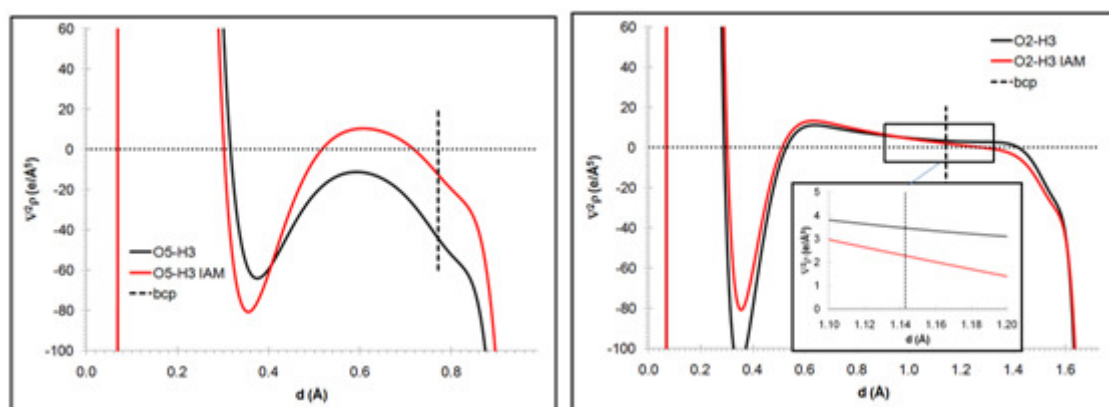


**Figure 4.7** Laplacian profile for the O5-H3 (left) and (O2-H3) interactions. The O atom is displayed on the left, while H atom is on the right. The dashed vertical line marks the position of the BCP. The inset shows an enlargement of the region next to the BCP.

The last kind of interactions revealed by the topological analysis of the electron density is the H...O hydrogen bond. They can be divided in two categories: O-H...O taking place between formate ions oxygen and water hydrogen, and C-H...O taking place between formate ions hydrogen and water oxygen (Table 4.5 and Table 4.6). As illustrated in the introduction of this chapter, the first ones (the shortest) are the most interesting ones to analyze due to the possibility of their involvement in the propagation of the magnetic information in the structure.

**Table 4.5** Topological parameters for the O-H...O interactions BCPs

Bond	d (Å)	AIL <sub>A-bcp</sub> (Å)	AIL <sub>bcp-B</sub> (Å)	$\rho(e/\text{Å}^3)$	$\nabla^2 \rho (e/\text{Å}^5)$	$\epsilon$
O2...H3	1.7315	1.1428	0.6074	0.291	3.467	0.033
O1...H6	1.7649	1.1564	0.6257	0.283	3.316	0.025
O4...H5	1.7723	1.1597	0.6320	0.264	3.292	0.034
O3...H4	1.7807	1.1647	0.6344	0.261	3.234	0.038

**Table 4.6** Topological parameters for the various C-H...O interactions BCPs.

Bond	d (Å)	AIL <sub>A-bcp</sub> (Å)	AIL <sub>bcp-B</sub> (Å)	$\rho(e/\text{Å}^3)$	$\nabla^2 \rho (e/\text{Å}^5)$	$\epsilon$
O3...H2	2.3580	1.3884	1.0162	0.090	1.260	0.464
O1...H2	2.4859	1.4716	1.0405	0.072	0.901	0.215
O4...H1	2.5620	1.5035	1.0986	0.058	0.781	0.458
O5...H1	2.7248	1.6481	1.0899	0.040	0.488	0.021
O6...H1	2.9005	1.6866	1.2801	0.031	0.430	0.241

If the analysis of the bonding interactions is conducted considering also the electron energy density<sup>61</sup> it can be seen how, rather than simply closed shell, all the Zn-O and the H-bond interactions belong to the so-called “transit region” where ionic and covalent character are somewhat competitors.

Prompted by this new result, the Source Function has been evaluated to gain further insight on this kind of interaction. While it was hidden in the “simple” analysis based on the sign of the Laplacian, through the SF it is found that, for every Zn-O interaction, the atoms directly involved in the bonding provides only 60% of the total electron density which is recovered at the BCP (in almost equal amounts, ~30%). The remaining is actually provided by all the other atoms, including carbons contributing for ~10%. While this analysis is still ongoing, it can be a definite sign of the existence of a  $\pi$ -delocalization scheme connecting the Zn atoms.

## 5. Conclusions

The charge density of the coordination polymer Zn(HCOO)<sub>2</sub>(H<sub>2</sub>O)<sub>2</sub> has been modeled based on two X-ray diffraction data sets obtained at 15 and 100 K. Furthermore, densities from periodic DFT

calculations based on the experimental geometry have been obtained. In general there is a good agreement between the two experimental and the theoretical densities. The charge density of Zn in various compounds reported in the literature and the description is quite varying from highly spherical to distorted ions. The charge density of the title compound show overall quite spherical Zn atoms. However differences between the two experimental descriptions are found. It is clear that the description of Zn features require extremely high quality data as several models yields similar residuals but varying description of the charge density. The deformation density maps show accumulations towards the oxygen atoms of the ligands. This is also found in the theoretical models and supports the idea of covalent character in this interactions. This is also strengthened by the analysis of the electron energy density and of the Source Function.

## Chapter 5

### Conclusions and Future Work

The charge density of  $\text{FeX}_2$  marcasitic compounds, of crystalline  $\text{K}_2\text{SO}_4$  and of a reference compound for magnetically active coordination polymers have been analysed from both the experimental and crystallographic point of view. In the two cases where the work took the moves from the need to disentangle the ambiguities arising from the experimentally derived electron density, *ab-initio* calculations proved to be able to aid, at least qualitatively. In many cases, especially through the topological analysis of  $\rho$ , the role of theory has been also a quantitative one. This was, for example, the case of  $\text{K}_2\text{SO}_4$ . The presence of heavy elements and extinction effects masked the fine mechanisms related to the charge polarization within the oxygen atoms themselves. Of course also the opposite is true, as that of theory and experiment in charge density analysis is a synergic and strongly intertwined work. A finer analysis of the multipole-modeled  $\rho$  would hopefully provide support to the mechanism governing the bonding interactions in  $\text{FeX}_2$  compounds.

Even if almost completed, the analysis of  $\text{Zn}(\text{HCOO})_2(\text{H}_2\text{O})_2$  just scratched the surface of what's hidden within this family of compounds. Presently, analyses on the Mn and Fe containing compounds are in an advanced state.

Lastly, even if unfortunately they haven't found space in these pages, two others projects should be mentioned, both dealing with crystals characterized by high disorder. The first one, in collaboration with PhD student Mette Sjøberg and postdoc Henrik F. Clausen (Århus university), is aimed at unraveling the properties of hydroquinone giving rise, when in its crystal form, to a host-guest structure able to imprison small solvent molecules like methanol and acetonitrile. The second one,

in collaboration with Dr. Marlena Gryl (Jagiellonian university), is aimed at evaluating the bonding features in co-crystals of organic molecules characterized by non-linear optical properties.

## References

---

- [1] Bentien, A.; Johnsen, S.; Madsen, G. K. H.; Iversen, B. B.; Steglich, F. *Eur. Phys. Lett.* **2007**, 80, 17008-17012
- [2] Bentien, A.; Madsen, G. K. H.; Johnsen, S.; Iversen, B. B., *Phys. Rev. B.* **2006**, 74, 205105
- [3] Sun, P.; Søndergaard, M.; Sun, Y.; Johnsen, S.; Iversen, B. B.; Steglich, F. *Appl. Phys. Lett.* **2011**, 98, 072105; Sun, P.; Søndergaard, M.; Iversen, B. B.; Steglich, F. *Ann. Phys.* **2011**, 523, 612–620; Sun, P.; Oeschler, N.; Johnsen, S.; Iversen, B.B.; Steglich, F., *Dalton Trans.* **2010**, 39, 1012-1019
- [4] Holseth, H.; Kjekshus, A. *Acta Chemica Scandinavica* **1968**, 22, 3284-3292
- [5] Dahl, E. *Acta Chemica Scandinavica* **1969**, 23, 2677-2684
- [6] Brostigen, G.; Kjekshus, A. *Acta Chemica Scandinavica* **1970**, 24, 1925-1940
- [7] Brostigen, G.; Kjekshus, A. *Acta Chemica Scandinavica* **1970**, 24, 2983-2992
- [8] Brostigen, G.; Kjekshus, A.; Rømming, C. *Acta Chemica Scandinavica* **1973**, 27, 2791-2796
- [9] xxx *Acta Chemica Scandinavica*. **A28** (1974) 996
- [10] xxx *Acta Chemica Scandinavica*. **24** (1970) 2993
- [11] xxx *Acta Chemica Scandinavica*. **24** (1970) 3309
- [12] Goodenough, J.B. *Journal of Solid State Chemistry* **1972**, 5, 144-152
- [13] Hullinger, F.; Mooser, E. *Journal of Physics and Chemistry of Solids* **1965**, 26, 429-433
- [14] *Angew. Chem. Int. Ed.* **39** (2000) 2408
- [15] *J. Mater. Chem.* **18** (2008) 2090

- 
- [16] Dovesi, R.; Saunders, V.R.; Roetti, C.; Orlando, R.; Zicovich-Wilson, C.M.; Pascale, F.; Civalleri, B.; Doll, K.; Harrison, N.M.; Bush, I.J.; D'Arco, Ph.; Llunell, M. *CRYSTAL06 User's Manual*, University of Torino, Torino, **2006**
- [17] Weigend, F.; Ahlrichs, R. *Physical Chemistry Chemical Physics* **2005**, 7, 3297
- [18] Ahlrichs, R.; May, K. *Physical Chemistry Chemical Physics* **2000**, 2, 943
- [19] M. Dolg, U. Wedig, H. Stoll, H. Preuss, J. Chem. Phys. 86, 866 (1987); J.M.L. Martin, A. Sundermann, J. Chem. Phys. 114, 3408 (2001); B. Metz, H. Stoll, M. Dolg, J. Chem. Phys. 113, 2563 (2000)
- [20] Perdew, J. P.; Burke, K.; Ernzerhof, M. *Physical Review Letters* **1996**, 77, 3865
- [21] a) Becke, A. D. *Journal of Chemical Physics* **1993**, 98, 5648; b) Perdew, J. P. *Electronic Structure of Solids*, Akademie Verlag, Berlin (**1991**); c) Perdew, J. P.; Wang, Y. *Physical Review B* **1986**, 33, 8800; d) Perdew, J. P.; Wang, Y. *Physical Review B* **1989**, 40, 3399; e) Perdew, J. P.; Wang, Y. *Physical Review B* **1992**, 45, 13244
- [22] Boda, G.; Stenstrom, B.; Sagredo, V.; Beckman, O. *Physica Scripta* **1971**, 4, 132-134
- [23] Sithole, H.M.; Nguyen-Manh, D.; Pettifor, D.G.; Ngoepe, P.E. *Molecular Simulation* **1999**, 22 31-37
- [24] *App. Phys. Express* **2** (2009) 091102
- [25] *Eur. Phys. J. B* **53** (2006) 205
- [26] *Phys. Rev. B* **74** (2006) 205105
- [27] *App. Phys. Express* **2** (2009) 091102
- [28] *Phys. Rev. B* **74** (2006) 205105
- [29] Bader, R. F. W. *Atoms in molecules. A quantum theory*. **1990**, Oxford University Press, Oxford, UK

- 
- [30] Bianchi, R.; Gatti, C.; Adovasio, V.; Nardelli, M. *Acta Cryst. B* **1996**, *52*, 471–478.
- [31] Macchi, P.; Sironi, A. *Coordination Chemistry Review* **2003**, *238*, 383-412
- [32] Gatti, C. *Z. Krist.* **2005**, *220*, 399-457
- [33] Cortéz-Guzmán, F. ; Bader, R.F.W. *Coordination Chemistry Review* **2005**, *249*, 633-662
- [34] Scherer, W.; McGrady, G. S. *Angew. Chem. Int. Ed.* **2004**, *43*, 1782-1806
- [35] Saito, Y. *Inorganic Molecular Dissymmetry*. Springer-Verlag, **1979** New York
- [36] Koritsanszky, T. S.; Coppens, P. *Chem. Rev.* **2001**, *101*, 1583–1627.
- [37] Bader, R.F.W. *Coord. Chem. Rev.* **2000**, *197*, 71–94.
- [38] Gillespie, R.J. *Canadian Journal of Chemistry* **1992**, *70*, 742-750
- [39] Lewis, G.N. *J. Am. Chem. Soc.* **1916**, *38*, 762-785.
- [40] (a) Cioslowski, J.; Mixon, S.T. *Inorg. Chem.* **1993**, *32*, 3209-3216. (b) Wang, Y.; Chang, N. L.; Pai, C. T. *Inorg. Chem.* **1990**, *29*, 3256-3259. (c) Lee, C. R.; Tang, T.-H.; Chen, L.; Wang, Y. *Chem. Eur. J.* **2003**, *9*, p. 3112-3121. (d) Bats, J.W.; Coppens, P.; Koetzle, T. F. *Acta Cryst.* **1977**, *B33*, 37-45. (e) Figgis, B. N.; Khor, L.; Kucharski, E. S.; Reynolds, P. A. *Acta Cryst.* **1992**, *B48*, 144-151. (f) Figgis, B. N.; Iversen, B. B.; Larsen, F. K.; Reynolds, P. A. *Acta Cryst.* **1993**, *B49*, 794-806.
- [41] (a) Dobado, J. A.; Martínez-García, H.; Molina, J.; Sundberg, M. R.; *J. Am. Chem. Soc.* **1999**, *121*, 3156-3164. (b) Dobado, J. A.; Martínez-García, H.; Molina, J.; Sundberg, M. R.; *J. Am. Chem. Soc.* **1998**, *120*, 8461-8471.
- [42] Love, I. *J. Phys. Chem. A* **2009**, *113*, 2640-2646.

- 
- [43] (a) Mezey, P. G.; Haas E. C. *J. Chem. Phys.* **1982**, *77*, 870-876. (b) Mayer, I. *J. Mol. Struct. THEOCHEM* **1987**, *149*, 81-89. (c) Yu, W.; Guo, L. W.; Lin, H. C.; Kao, C. T.; Tsai, C. J.; Bats, J. W. *Inorg. Chem.* **1988**, *27*, 520-523.
- [44] Cioslowski, J.; Surján P. R. *J. Mol. Struct. THEOCHEM* **1992**, *87*, 9-33.
- [45] Ojima, K.; Nishihata, Y.; and Sawada, A. *Acta Cryst.* **1995**, *B51*, 287-293.
- [46] (a) Clausen, H. F.; Overgaard, J.; Chen, Y. S.; Iversen, B. B., *J. Am. Chem. Soc.* **2008**, *64*, 7988-7996. (b) Poulsen, R. D.; Bentien, A.; Chevalier, M.; Iversen, B.B., *J. Am. Chem. Soc.* **2005**, *127*, 9156-9166. (c) Coppens, P.; Larsen, F. K.; Iversen, B. B. *Coord. Chem. Rev.* **2004**, *249*, 179-195.
- [47] Volkov, A.; Macchi, P.; Farrugia, L. J.; Gatti, C.; Mallinson, P.; Richter, T.; Koritsanszky, T. *XD2006 - A Computer Program Package for Multipole Refinement, Topological Analysis of Charge Densities and Evaluation of Intermolecular Energies from Experimental and Theoretical Structure Factors*; **2006**.
- [48] Gatti C. TOPOND08 – An electron density topological program for systems periodic in N (N = 1-3) dimensions.
- [49] Morse, M.; Cairns S. S. *point theory in global analysis and differential topology; an introduction*. Pure and applied mathematics a series of monographs and textbooks. Academic Press: New York, 1969.
- [50] (a) Bader, R.F.W., Gatti, C. *Chem. Phys. Lett.* **1998**, *287*, 233 (b) Gatti, C., Lasi, D. *Faraday Discuss.* **2007**, *135*, 55; (c) Farrugia, L. J.; Macchi, P. *J. Phys. Chem A.* **2009**, *113*, 10058-10067; (d) Gatti, C. *Struct. Bond.* **2011**, *1* DOI: 10.1007/430\_2010\_31 2.. (e) Lo Presti, L.; Gatti C. *Chem. Phys. Lett.* **2009**, *476*, 308-316.
- [51] Weng, D.-F., Wang, Z.-M. & Gao, S. (2011). *Chem. Soc. Rev.* **40**, 3157-3181; Sculley, J., Yuan, D. & Zhou, H.-C. (2011). *Energ Environ Sci* **4**, 2721-2735; Ranocchiari, M. & van

- 
- Bokhoven, J. A. (2011). *Phys. Chem. Chem. Phys.* **13**, 6388-6396; Meek, S. T., Greathouse, J. A. & Allendorf, M. D. (2011). *Adv. Mater. (Weinheim, Ger.)* **23**, 249-267; Martinez, C. & Corma, A. (2011). *Coord. Chem. Rev.* **255**, 1558-1580 Dechambenoit, P. & Long, J. R. (2011). *Chem. Soc. Rev.* **40**, 3249-3265; Coudert, F.-X., Boutin, A., Jeffroy, M., Mellot-Draznieks, C. & Fuchs, A. H. (2011). *ChemPhysChem* **12**, 247-258.; Zhou, W. (2010). *Chem. Rec.* **10**, 200-204; Ma, S. & Zhou, H.-C. (2010). *Chem. Commun. (Cambridge, U. K.)* **46**, 44-53; Lock, N., Wu, Y., Christensen, M., Cameron, L. J., Peterson, V. K., Bridgeman, A. J., Kepert, C. J. & Iversen, B. B. (2010). *J. Phys. Chem. C* **114**, 16181-16186; Peterson, V. K., Kearley, G. J., Wu, Y., Ramirez-Cuesta, A. J., Kemner, E. & Kepert, C. J. (2010). *Angew Chem Int Edit* **49**, 585-588.
- [52] Edgar, M., Mitchell, R., Slawin, A. M. Z., Lightfoot, P. & Wright, P. A. (2001). *Chemistry – A European Journal* **7**, 5168-5175
- [53] Clausen, H. F., Poulsen, R. D., Bond, A. D., Chevallier, M. A. S. & Iversen, B. B. (2005). *J. Solid State Chem.* **178**, 3342-3351.
- [54] Poulsen, R. D., Bentien, A., Chevalier, M. & Iversen, B. B. (2005). *J. Am. Chem. Soc.* **127**, 9156-9166.; Poulsen, R. D., Bentien, A., Graber, T. & Iversen, B. B. (2004). *Acta Crystallogr A* **60**, 382-389; Clausen, H. F., Overgaard, J., Chen, Y. S. & Iversen, B. B. (2008). *J. Am. Chem. Soc.* **130**, 7988-7996.
- [55] Jørgensen, M. R. V., Clausen, H. F., Christensen, M., Poulsen, R. D., Overgaard, J. & Iversen, B. B. (2011). *Eur. J. Inorg. Chem.* 549-555; Clausen, H. F., Overgaard, J., Chen, Y. S. & Iversen, B. B. (2008). *J. Am. Chem. Soc.* **130**, 7988-7996.
- [56] Osaki, K., Nakai, Y. & Watanabe, T. (1963). *J. Phys. Soc. Jpn.* **18**, 919.
- [57] Flippin, R. B. & Friedberg, S. A. (1963). *J. Chem. Phys.* **38**, 2652-2657; Abe, H. & Matsuura, M. (1964). *J. Phys. Soc. Jpn.* **19**, 1867-1880; Abe, H., Matsuura, M., Morigaki, H., Yamagata,

- 
- K. & Torii, K. (1964). *J. Phys. Soc. Jpn.* **19**, 775-776. , R. D. & Friedberg, S. A. (1968). *Phys. Rev.* **165**, 680-686.
- [58] Pierce, R. D. & Friedberg, S. A. (1968). *Phys. Rev.* **165**, 680-686
- [59] Poulsen, R. D., Jorgensen, M. R. V., Overgaard, J., Larsen, F. K., Morgenroth, W. G., Graber, T., Chen, Y. S. & Iversen, B. B. (2007). *Chem.--Eur. J.* **13**, 9775-9790
- [60] Shi, Z.; Boyd, R. J.; *J. Chem. Phys.* **88**, 4375 (1988).
- [61] Espinosa, E.; Alkorta I.; Elguero, J.; Molins, E.; *J. Chem. Phys.* **117**, 5529 (2002).